KRONOS FUSION ENERGY

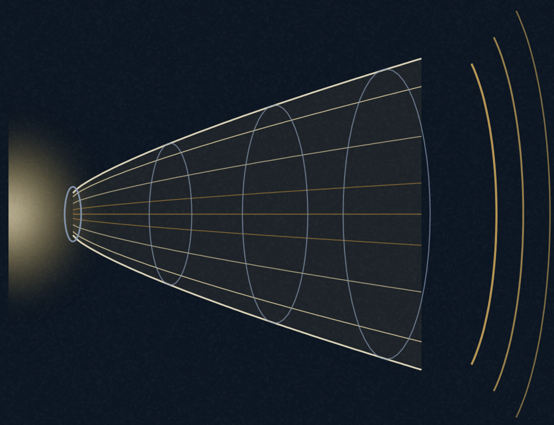

PAPER 1.4 · THE KRONOS 2026 SERIES

Direct Energy Conversion for a D–^{3}He Tandem-Mirror Burner: Recovering Charged-Particle Power Directly Without a Thermal Cycle

A deuterium–helium-3 (D–He) tandem-mirror burner puts most of its fusion power into charged particles, so it admits an option a tokamak does not: recover the exhaust…

Read it live — 3-D model · physics validator · film series

BY P I FORD AND G L KULCINSKI

2026 · EDITORIAL EDITION

THE OFFICIAL RECORD

What this document is, and how to read its numbers

This is a combined editorial. It gathers, in one volume, the two design studies Kronos Fusion Energy released in 2026 — a compact spherical-tokamak tritium/helium-3 breeder and a deuterium–helium-3 tandem-mirror generator — together with the intellectual-property estate, the people, and, in the internal edition, the full commercial case. The scientific text is the same text that appears in the arXiv preprints and the journal submissions; the editorial adds the apparatus a reader needs to hold the whole program at once, and nothing in the physics is altered to fit it.

THE HONESTY STANCE IS THE ASSET

Every headline quantity carries an **evidence class** — DERIVED RECOMPUTED MEASURED REQUIREMENT — and, where a number is a modelled extrapolation rather than a demonstrated value, it is labelled as such and its downside is shown next to it. Several quantities in the underlying corpus moved after first publication; where a value has been withdrawn or restated, the record says so plainly. This is deliberate: a diligence team will find the load-bearing assumptions, so the document surfaces them first.

TWO EDITIONS

This volume is issued in two editions. The **public edition** (light) carries the physics and the design only — no dollar, price, or per-kilogram figure appears anywhere in it. The **internal edition** (dark) adds the economics, the funding architecture, and the defense-commercial analysis, and is marked *Confidential* accordingly; it is not for public distribution. Where the commercial case rests on a modelled assumption rather than a demonstrated one, it is labelled as such and its downside is shown alongside it, on the same terms as the physics.

TITLE	The Kronos Fleet — Hyperion · Aegis · MetroVolt: A Combined Design & Commercialization Study
AUTHOR	Priyanca Ford, Founder & CEO, on behalf of Kronos Fusion Energy
EDITION	2026 Combined Editorial · first issue
COMPANION WORKS	The five-paper arXiv drop — (1) Breeder, (2) Burner, (3) REBCO magnet & tape, (4) Direct Energy Conversion, (5) AI/ML/Quantum control — with matching numbered Zenodo deposits, plus the IOP journal and IAEA-FEC submissions. Patents were filed before the drop.
NAMING	Hyperion = the breeder; Aegis (defense) and MetroVolt (data-center) = one generator in two housings. Internal mode letters (D1, L) do not appear on public surfaces.
STATUS	Conceptual design & simulation study. Nothing herein is a construction commitment.

HOW TO READ THIS VOLUME

The fleet at a glance, and the way its numbers are marked

This volume opens with *Orientation*, presents the five research papers as a bound sequence, and closes with the *Apparatus*. *Foundations* sets out the three general results both machines rest on. *Paper One* is the Hyperion breeder; *Paper Two* the Aegis / MetroVolt generator; *Papers Three, Four and Five* are the enabling science — high-field REBCO magnets and tape, direct energy conversion, and the AI / ML / quantum control stack. A *Digital Twin & 3-D Model* part follows, then the *Environmental* profile. The *Economics* and levelized cost and the *Business Case* and diligence record appear in the internal edition only; the *Simulations* proof record and the Apparatus — patent portfolio, team, limitations, and sources — close both editions.

THE FLEET AT A GLANCE

	HYPERION	AEGIS	METROVOLT
Role	Strategic-isotope foundry	Defense installation power	Campus power
Machine	**Spherical tokamak**	**Tandem mirror**	**Tandem mirror**
Fuel	Deuterium–tritium	Deuterium–helium-3	Deuterium–helium-3
Delivers	Tritium · ^{3}He · 14 MeV n	Resilient installation power	Firm campus power
Physics bar	**Fusion gain only**	Closure (gates named)	Closure + lunar ^{3}He
In the fleet	Breeds the fuel	Proves the generator	Commercial destination

HOW THE NUMBERS ARE MARKED

Every headline quantity carries an evidence class — DERIVED from first principles, RECOMPUTED from raw data, MEASURED in hardware, or a REQUIREMENT yet to be met. Financial figures carry a case label and are confined to the internal (confidential) edition. Values that moved after first publication are shown as withdrawn or restated rather than quietly changed. A capability you can evaluate is one whose limits are on the page.

ABSTRACT

Direct Energy Conversion for a D–³He Tandem-Mirror Burner: Recovering Charged-Particle Power Directly Without a Thermal Cycle

A deuterium–helium-3 (D–^{3}He) tandem-mirror burner puts most of its fusion power into charged particles, so it admits an option a tokamak does not: recover the exhaust electrostatically, as electricity, without a thermal cycle or a turbine on the direct channel. This paper is the flagship, review-length treatment of that option for the Kronos burner (engineering gain $Q_E = 1.318$ at $P_{\text{fus}} = 4298.5$ MW, neutron fraction $f_n = 5.44\,\%$, plug potential $e\phi_i = 248.75$ keV, on the open field lines downstream of a $26.49\,\text{T}$ plug coil that is a distinct magnet from the breeder's $16.84\,\text{T}$ centrepost). We write the governing physics as explicit, step-by-step derivations: the D–^{3}He energetics and the Bosch–Hale reactivity that fix the operating point; the Pastukhov ambipolar confinement that sets the axial end-loss channel; the synchrotron-transport calculation that pins the electron temperature; the Stix collisional slowing-down partition, which shows that at a reactor electron temperature $T_e \approx 89.7$ keV the 14.68 MeV fusion proton is born more than an order of magnitude above its critical energy and hands $\approx 83\,\%$ of its energy to the electrons, so that the thermalized axial exit carries an *electron-dominant* split ($\approx 55.5\,\%$ electron/thermal against $\approx 44.5\,\%$ directed ion) that inverts the received birth-spectrum picture and holds across 20–200 keV; the multi-stage electrostatic collector and its Child–Langmuir space-charge limit; the travelling-wave converter for the proton channel; and a quasineutral two-species expander that recovers the directed electron stream against the ambipolar potential of the expansion. We resolve the direct-converter efficiency into a defensible ladder — frozen conservative anchor $\eta_{\text{dec}} = 0.49$, floor 0.56, Moir–Barr design 0.70, ideal proton-only ceiling 0.85 — and place it correctly in the plant balance: booked at the design value the burner delivers $P_{\text{out}} = 3522.0$ MWe against $P_{\text{in}} = 2672.0$ MWe ($+850.0$ MWe net, recirculating fraction 0.759), but the net-positive knee sits at $\eta_{\text{dec}} \approx 0.52$, so *conversion is a bounded upside lever, not the closure mechanism* — closure is gated by the recirculating plug power, and central-cell length, not converter efficiency, buys the net margin ($+104/+850/+2832$ MWe at $55/440/1400\,\text{m}$). A 40,000 -sample global uncertainty study returns $Q_E = 1.317 \pm 0.14$ with $P(Q_E > 1) = 1.0$, and a Saltelli–Sobol decomposition identifies the plug density ratio ($S_1 = 0.41$) and central-cell β (rank correlation 0.93), not η_{dec}, as the leading drivers. We give the GPU-HPC methodology (the codes, not dollars), map the converter onto the two products — Aegis forward-base (grid-independent black-start in $\approx 42\,\text{s}$) and MetroVolt data-center (HVDC-native $88.1\,\%$ source-to-chip against $75.9\,\%$ for a conventional AC chain) — and benchmark against the published venetian-blind, travelling-wave, expander, and mirror-revival literature. Kronos has built no converter; every headline quantity is a frozen anchor in the de-risking register[R0].

Open-access deposit (code & data, CC BY 4.0): DOI 10.5281/zenodo.22645700 · Zenodo community *kronos_fusion_energy*. Explore it live: interactive 3-D model · physics validator.

Keywords: direct energy conversion · deuterium--helium-3 · tandem mirror · ambipolar potential · Pastukhov confinement · travelling-wave converter · quasineutral expander · HVDC-native power · advanced-fuel fusion · uncertainty quantification

CONTENTS

Table of Contents

NOMENCLATURE

Symbols, units, and the names of things

Q	plasma (fusion) gain, P_{fus}/P_{aux}
Q_E	engineering gain, net electric out / recirculating in
H_{98}	confinement enhancement over the IPB98(y,2) scaling
Z_{eff}	effective ion charge
c_{ee}	electron–electron bremsstrahlung leading coefficient, 2.120022 (exact)
τ_E	energy confinement time
I_p	plasma current
R_0, a	major radius, minor radius
κ, δ	elongation, triangularity
β_N	normalized plasma beta (Troyon-normalized)
TBR	tritium breeding ratio
DEC	direct energy conversion
CF	plant capacity factor (availability)
FOAK / NOAK / BOAK	first / n^{th} / best of a kind
Hyperion	the ST breeder (internal: Mode D2)
Aegis	the generator, defense/installation housing (internal: Mode M)
MetroVolt	the generator, data-center housing (Mode M)

Nomenclature tocsectionNomenclature

@L>X@ SYMBOL	DEFINITION
$E_p,\ E_\alpha$	birth energy of the D–^{3}He proton (14.68 MeV) and ^{4}He (3.67 MeV)
E_c	Stix critical energy (fast-ion equipartition between background ions and electrons)
E_0	fast-ion birth energy entering the slowing-down partition
$f_e,\ G(x)$	electron energy-share fraction; ion share integral $G(x) = x^{-1}\int_0^x \mathrm{d}y/(1+y^{3/2})$
$f_n,\ f_{\rm dir}$	neutron fraction of fusion power ($5.44\,\%$); charged fraction of exhaust routed to DEC (0.4945)
$e\phi_i$	ambipolar (plug) potential barrier confining central-cell ions
$T_i,\ T_e$	central-cell ion and electron temperature
$R_{\rm mc},\ R_{\rm exp}$	plug mirror ratio; magnetic-expansion (flux-expansion) ratio of the end expander
ℓ_c	central-cell length
$\langle\sigma v\rangle$	Maxwellian thermal reactivity (Bosch–Hale)
$\tau_s,\ \tau_\parallel$	collisional slowing-down time; Pastukhov axial-confinement time
n^*	synchrotron optical-depth cutoff harmonic
$\eta_{\rm dec},\ \eta_{\rm th},\ \eta_{\rm grid}$	direct-converter efficiency; thermal-cycle efficiency; grid transparency factor
$\eta_{\rm coll}$	multi-stage electrostatic collector efficiency
$P_{\rm fus},\ P_{\rm ax},\ P_{\rm exh}$	fusion power; charged axial end-loss power; total exhaust power
$P_{\rm brems},\ P_{\rm syn},\ P_{\rm rad}$	bremsstrahlung, reabsorbed synchrotron, total radiated power
$P_{\rm out},\ P_{\rm in}$	gross electric output; recirculating electric input (heating/plug drive)
$Q,\ Q_E$	reaction energy release; engineering (net-electric) gain, $P_{\rm out}/P_{\rm in}$
ε	recirculating fraction $P_{\rm in}/P_{\rm out}$
$J_{\rm CL}$	Child–Langmuir space-charge-limited current density
V_k	retarding potential of the k-th collector electrode
μ	first adiabatic invariant $mv_\perp^2/2B$
S_1	first-order Saltelli–Sobol sensitivity index

§ 1

Introduction

WHY DIRECT ENERGY CONVERSION, AND WHY HERE

A magnetically confined fusion reactor that burns a deuterium–tritium (D–T) plasma puts $\approx 80\,\%$ of its yield into 14.1 MeV neutrons, which can only be captured as heat and run through a Rankine or Brayton cycle; the conversion to electricity is Carnot-bounded, and the machine inherits the whole thermal-plant apparatus. A deuterium–helium-3 burner is different in kind. The primary reaction

$$\mathrm{D} + {}^{3}\mathrm{He} \longrightarrow {}^{4}\mathrm{He}\,(3.67\ \mathrm{MeV}) \ + \ p\,(14.68\ \mathrm{MeV}), \qquad Q = 18.35\ \mathrm{MeV},$$

releases its energy entirely in charged particles, and even with the parasitic D–D and D–T side reactions the neutron fraction of total fusion power at the Kronos operating point is only $f_n = 5.44\,\%$ [1]. A stream of charged particles can, in principle, be decelerated in an electrostatic field and delivered directly as electricity — *direct energy conversion* (DEC) — at an efficiency set by collector physics rather than by Carnot, and with the turbine hall deleted for the direct channel [2,10]. This is the single largest structural advantage of the advanced-fuel line, and it is why the Kronos burner is an open-ended linear device — a tandem mirror with a direct converter on the fanned-out field lines at each end — rather than a torus.

The idea is old. Post proposed periodic electrostatic and expander converters for mirror machines [5,10]; Moir and Barr designed and analysed the venetian-blind converter for D–T and advanced fuels, reaching $\approx 70\,\%$ collector efficiency in design [2], and Barr, Hamilton and Moir *measured* $65 \pm 7\,\%$ of the total ion power recovered at the beginning of a $100\,\mathrm{kV}$ beam pulse in a reduced-area beam direct converter [4]. The travelling-wave direct converter was demonstrated on real mirror end-loss ions on GAMMA-10 [30], and the D–^{3}He fuel-cycle reactor studies (ARTEMIS [29]) sketched the plant context. What has changed is that a compact, high-field D–^{3}He tandem mirror is now a concrete design point rather than a fuel-cycle sketch, so the converter can — and must — be specified against a real exhaust spectrum, a real recirculating power balance, and a real product. That is the purpose of this paper.

THE TANDEM-MIRROR BURNER IN ONE PARAGRAPH

The Kronos burner confines a long central cell ($\ell_c = 440\,\mathrm{m}$ at the ratified design unit) between two high-field end plugs [1,62]. An ambipolar electrostatic potential $e\phi_i$, generated at the plugs, exponentially enhances the axial confinement of central-cell ions (Pastukhov confinement [12,13,14]); at the design point $e\phi_i = 248.75$ keV with $\phi_i/T_i = 2.764$, and this exponential is what closes the burn. The plug field is produced by a no-insulation REBCO coil at a peak field of $26.49\,\mathrm{T}$ — a distinct, higher-field magnet from the breeder's $16.84\,\mathrm{T}$ centrepost, and the two must never be conflated [51,1]. Ions that do leak over the barrier, together with the 14.68 MeV fusion protons, flow out along the open field lines, fan out in a magnetic *expander*, and strike the direct converter. This paper takes the burner's frozen 0-D power balance as given (companion papers close it [49,50,52]) and asks the DEC question: what is actually in that exhaust, how is it recovered, at what efficiency, and how much does it matter to the plant.

THE MODERN MIRROR REVIVAL

The burner rides a genuine revival of the axisymmetric magnetic mirror, a line whose reactor prospects Ryutov set out decades ago [11]. High-field high-temperature-superconductor (HTS) mirrors now have a published physics basis — the Wisconsin HTS Axisymmetric Mirror (WHAM) [36], with beam-ion fusion gain analysed by a dedicated Fokker–Planck model [37] — and the gas-dynamic trap has demonstrated the electron-temperature and ambipolar-potential physics the plug relies on [38,39], together with the shear-flow vortex confinement that stabilises the axisymmetric configuration [40]. Simpler tandem configurations have been re-examined for high gain [16]. Direct conversion is the piece of the advanced-fuel mirror that has *not* been re-derisked at reactor scale in that revival; specifying it against a real burner power balance is where this paper sits.

PRIOR ART IN DIRECT ENERGY CONVERSION

Direct energy conversion has a fifty-year pedigree that a compact D–^{3}He burner inherits rather than invents. Post's early proposals covered both the periodic electrostatic converter and the expander/venetian-blind family for mirror machines [5,10], and the systematics of energy conversion for fusion were codified in Miley's monograph [6] and the reactor-physics texts of the period [7]. The venetian-blind converter was carried from concept to a $65 \pm 7\,\%$ measured recovery at $100\,\mathrm{kV}$ in the Barr–Hamilton–Moir beam direct converter [2,4,3], establishing the electrostatic branch as an engineering reality rather than a paper design. The travelling-wave branch matured later, on GAMMA-10, where deceleration of real mirror end-loss ions was demonstrated and the beam-bunching requirement quantified [30]. At the plant level, the D–^{3}He fuel-cycle reactor studies (ARTEMIS [29]) and the broader advanced-fuel programme [41,42] placed the converter in a fuel-cycle context. What no prior study did — and what this paper supplies — is a converter specified against a *measured-anchor* burner power balance, with the end-loss spectrum, the recirculating loop, and the two products all fixed, and with the converter efficiency treated as a ladder rather than a single number. The end-loss physics on the input side rests on Baldwin's review of the processes that set the loss channel [8] and on Pastukhov's collisional-barrier theory [12].

CONTRIBUTIONS AND ROADMAP

Six contributions follow. (i) We write the governing physics of the burner's DEC problem as explicit, step-by-step derivations (§2): the D–^{3}He energetics and Bosch–Hale reactivity, the Pastukhov end-loss channel, the synchrotron-pinned electron temperature, the Stix slowing-down partition, the electrostatic-collector deceleration and its space-charge limit, the travelling-wave converter, the quasineutral expander, and the plant power balance. (ii) We establish, from the slowing-down partition, that the dominant axial-loss channel at reactor temperature is a directed *electron* stream, not the $14.68\ \mathrm{MeV}$ proton — an inversion of the received picture that reframes what the converter must recover. (iii) We resolve the converter efficiency into a defensible ladder and place it correctly in the recirculating balance (§4), showing that DEC is a bounded upside lever whose net knee sits just above the frozen conservative anchor, so that closure is gated by the plug power, not by conversion. (iv) We quantify the sensitivity and uncertainty of the closure (§5) with one-at-a-time, global Monte-Carlo, and Saltelli–Sobol studies, and resolve the synchrotron model-form ambiguity that pins the operating point. (v) We benchmark against the published venetian-blind, travelling-wave, expander, and mirror-revival literature (§6). (vi) We give the GPU-HPC methodology (§3) and map the converter onto the two products, Aegis and MetroVolt (§4). Every quantitative claim traces to a frozen result in the Kronos Physics De-Risking Register [1]; serial identifiers (e.g. BU-L1-A10) are given inline so each number is auditable. Appendices 11–17 collect the longer derivations, numerical schemes, and parameter tables.

§ 2

Governing equations and the formal problem

D–^{3}HE ENERGETICS AND THE CHARGED-POWER FRACTION

The primary reaction 1 shares its 18.35 MeV between the two charged products by momentum conservation. In the centre-of-momentum frame the two products carry equal and opposite momenta, so the kinetic energy divides inversely with mass: with $m_p : m_\alpha \simeq 1:4$,

$$\frac{E_p}{E_\alpha} = \frac{m_\alpha}{m_p} \simeq 4, \qquad \frac{E_p}{E_p + E_\alpha} = \frac{14.68}{18.35} = 0.800,$$

so the proton carries 80 % of the charged birth energy (figure 1a). The volumetric fusion power for a Maxwellian central cell of ion densities $n_{\mathrm{D}}, n_{\mathrm{He3}}$ is

$$P_{\mathrm{fus}} = n_{\mathrm{D}}\, n_{\mathrm{He3}}\, \langle \sigma v \rangle_{\mathrm{D^3He}}(T_i)\, Q \;+\; P_{\mathrm{DD}} + P_{\mathrm{DT}},$$

with the reactivity $\langle \sigma v \rangle$ taken from the Bosch–Hale parameterization [23] (Appendix 12). The D–D branch and the D–T reaction on the small bred-tritium inventory supply the only neutrons. At the Kronos operating point the fusion power resolves by branch as in table 2 and figure 2: the aneutronic D–^{3}He channel carries 3868.0 MW, while the D–D (2.45 MeV) and residual D–T (14 MeV) channels together account for the 233.95 MW neutron budget, so

$$f_n \equiv \frac{P_n}{P_{\mathrm{fus}}} = \frac{233.95 \qquad \mathrm{MW}}{4298.5 \qquad \mathrm{MW}} = 0.0544,$$

and 94.56 % of the fusion power leaves as charged particles (figure 1b) — the raw material for direct conversion, and the reason the D–^{3}He line can site a burner where a D–T machine cannot [25,24]. The 14 MeV D–T line carries 60 % of the neutron *power* but only 21 % of the neutron *count*, the remainder at the 2.45 MeV D–D energy; this asymmetry sets the shielding basis for the neutron-lean housing but does not touch the direct-conversion feedstock [1,52].

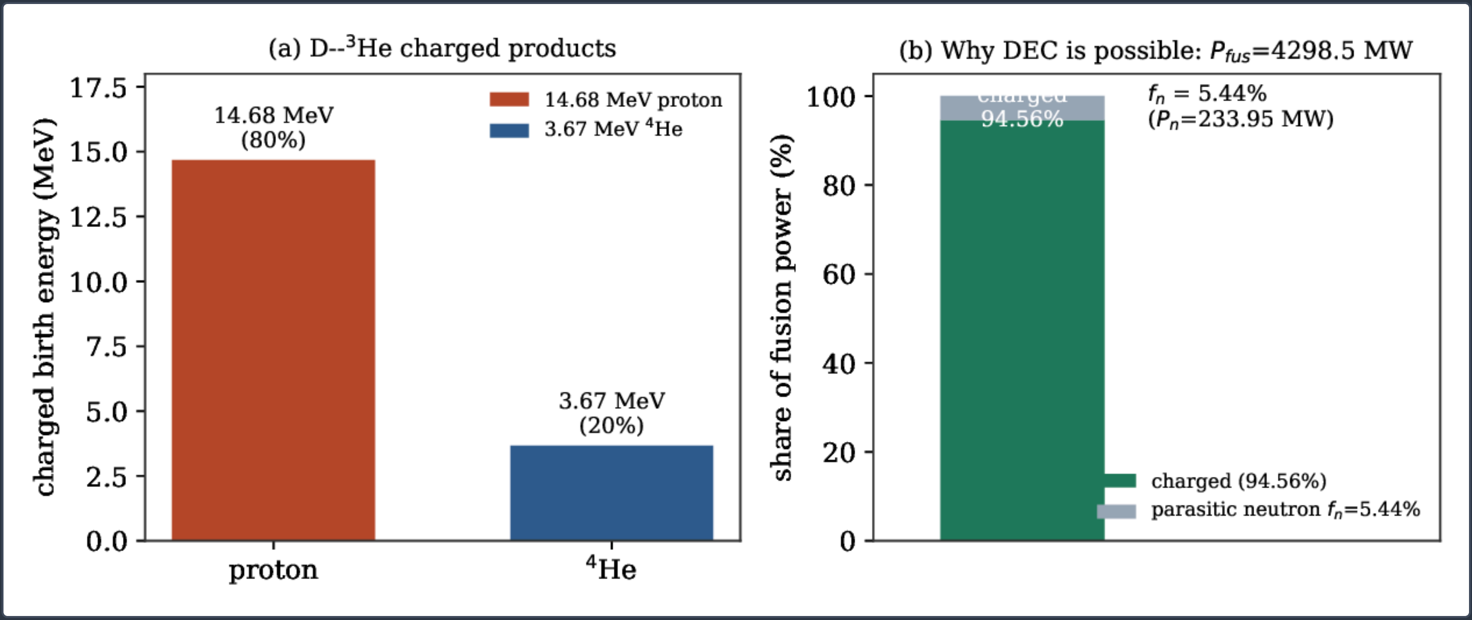

D–^{3}He energetics. **(a)** The 14.68 MeV proton carries 80 % of the charged birth energy, equation 2. **(b)** At the Kronos operating point only $f_n = 5.44$ % of fusion power ($P_{\mathrm{fus}} = 4298.5$ MW) is neutron; the charged remainder is the direct-conversion feedstock. Values are register anchors (BU-L1-A1) [1].

BRANCH	POWER (MW)	ROLE
D–^{3}He (aneutronic)	3868.0	direct-convertible charged products
D–D neutron (2.45 MeV)	124.8	neutron budget (count-dominant)
D–T (14 MeV)	176.0	neutron budget (power-dominant)
total P_{fus}	4298.5	$f_n = 5.44\,\%$, $P_n = 233.95$ MW

Fusion power by reaction branch at the frozen design point (ENV-A4-BU, BU-L1-A1 [1]); the branches sum to P_{fus} exactly.

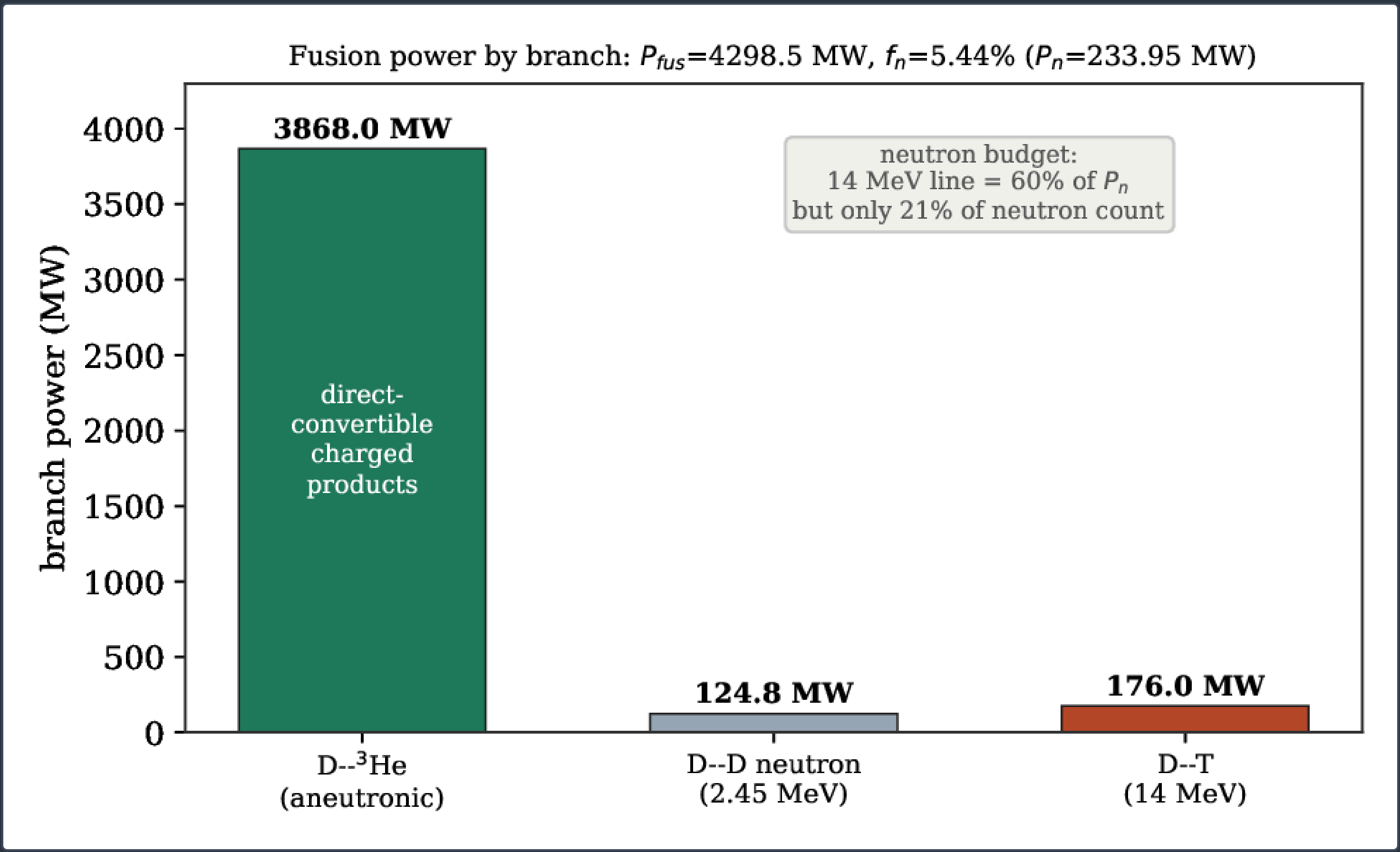

Fusion power resolved by reaction branch (table 2). The aneutronic D–^{3}He channel dominates (3868.0 MW); the neutron fraction is $f_n = 5.44\,\%$ ($P_n = 233.95$ MW). Branch powers reproduce to the stated digits (ENV-A4-BU) [1].

THE REACTIVITY THAT FORCES A HOT CENTRAL CELL

The D–^{3}He reactivity peaks near 250 keV and is more than an order of magnitude below D–T at the same temperature; both the Coulomb barrier ($Z_{\text{D}} Z_{\text{He}} = 2$) and the reaction physics push the optimum to high T_i (figure 3). The Bosch–Hale form,

$$\langle \sigma v \rangle = C_1\, \theta \sqrt{\frac{\xi}{m_r c^2\, T^3}}\, \exp(-3\xi), \qquad \xi = \left(\frac{B_G^2}{4\theta}\right)^{1/3}, \qquad \theta = \frac{T}{1 - \dfrac{T(C_2 + T(C_4 + TC_6))}{1 + T(C_3 + T(C_5 + TC_7))}},$$

with the Gamow constant B_G, reduced-mass energy $m_r c^2$, and fitted coefficients $C_1 \ldots C_7$ (Appendix 12), reproduces the measured cross-sections to within their experimental error over 0.5–190 keV [23]. At the burner's $T_i \approx 90$ keV the D–^{3}He reactivity is $\langle \sigma v \rangle \approx 1.5 \times 10^{-16}\,\text{cm}^3\,\text{s}^{-1}$; a burner therefore *must* run hot, which is what makes both the plug potential and the synchrotron loss (below) first-order design quantities. This is the same reactor-physics wall that motivates the p–^{11}B and colliding-beam alternatives [26,27], and the reason the tandem-mirror plug — not a higher reactivity — is the burner's binding lever.

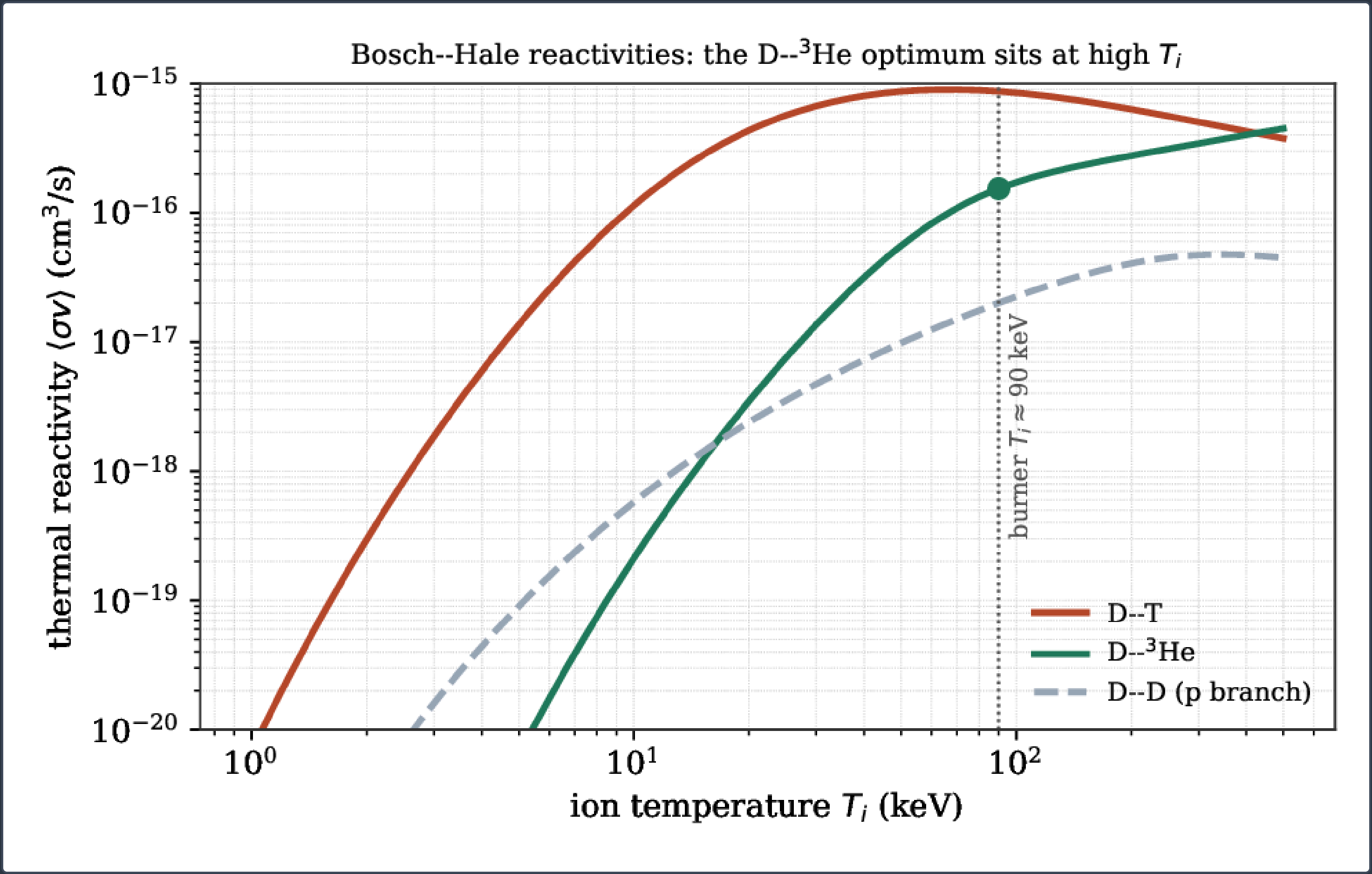

Bosch–Hale thermal reactivities 5 for D–T, D–^{3}He and the D–D proton branch [23]. The D–^{3}He optimum sits well above 100 keV; the burner runs at $T_i \approx 90$ keV (marked), which is what forces the hot central cell and the high plug potential.

THE END-LOSS CHANNEL: PASTUKHOV AMBIPOLAR CONFINEMENT

Central-cell ions are confined not only by the mirror ratio $R_{\rm mc}$ but by the electrostatic barrier $e\phi_i$ raised at the plugs. The confinement of a species held by a potential well ϕ in a mirror of ratio R is a loss-cone problem: a particle escapes only when pitch-angle scattering carries it into the region of velocity space that is simultaneously above the potential barrier and inside the loss cone. Solving the bounce-averaged Fokker–Planck equation for that boundary layer (Appendix 11) gives the Pastukhov axial-confinement time in the Cohen–Rensink corrected form [12,13],

$$\tau_{\parallel} \simeq \tau_s\, g(R)\, \frac{e\phi_i}{T_i} \exp\!\left(\frac{e\phi_i}{T_i}\right) \Big/ \ln\!\left(\tfrac{R+1}{1}\right),$$

where τ_s is the ion–ion collision time and $g(R)$ a slowly varying $O(1)$ mirror function. The exponential in 6 is the whole game (figure 4): at $\phi_i/T_i = 2.764$ the barrier multiplies the confinement by more than an order of magnitude, which is why the plug potential — not the converter — is the burner's binding lever [1,52]. An ion that does escape crosses the barrier and arrives at the expander with a directed axial energy of order $e\phi_i$ plus a few T_i, populating a central-cell end-loss spectrum in the 253–513 keV window (§2.6, figure 8); the 14.68 MeV fusion protons form a separate, monoenergetic high channel. These two populations are what the converter train must sort and decelerate.

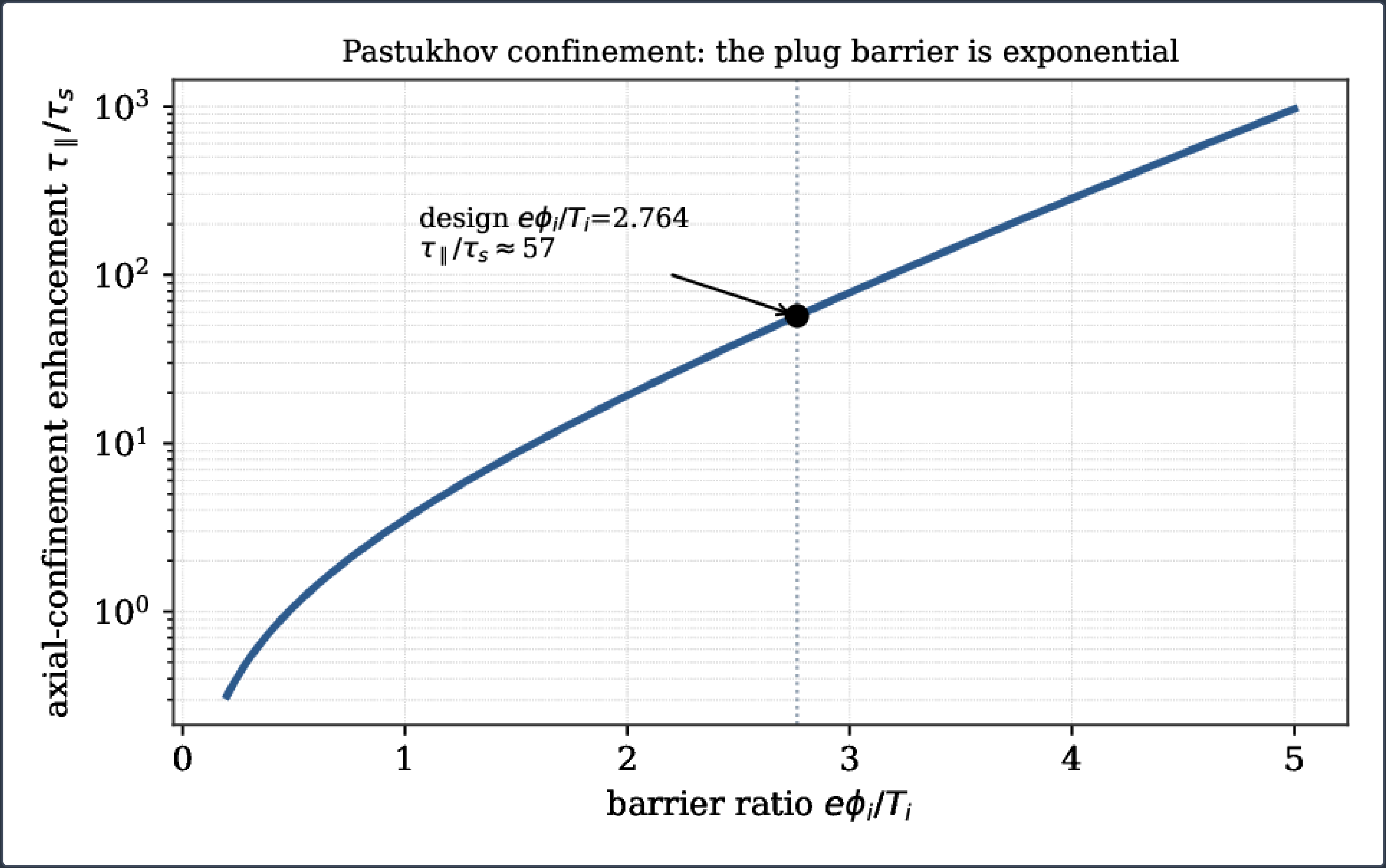

Pastukhov confinement, equation 6. The ratio $\tau_\parallel/\tau_s$ rises exponentially with the barrier ratio $e\phi_i/T_i$; at the design value **2.764** the plug enhances axial confinement by more than an order of magnitude. The plug potential, not the converter, is the binding lever.

THE SYNCHROTRON-PINNED ELECTRON TEMPERATURE

The slowing-down partition below depends sensitively on T_e, so the operating temperature must be fixed before the converter feedstock can be computed. In a hot, strongly magnetized electron population the dominant electron-energy sink is cyclotron (synchrotron) radiation, but the plasma is optically thick to the low harmonics that carry the power, so the escaping loss is neither the optically-thin emission nor a fixed fraction of P_{fus}. The escaping power is the emission integrated only above the cutoff harmonic n^* at which the optical depth $\tau_{n^*} \sim 1$; a relativistic Maxwell–Jüttner harmonic-transport calculation with wall reflectivity R_w (the Albajar–Johner–Granata, "AFJ", framework [32], resting on the electron-cyclotron emission/absorption theory of [33]) gives, at the design point,

$$P_{\text{syn}} = 1803 \quad \text{MW (AFJ, reabsorbed)}, \qquad P_{\text{rad}} = 2546 \quad \text{MW}, \qquad n^* \approx 10.4,$$

against 919 MW from the Trubnikov formula [20] and an unphysical 66,677 MW optically-thin estimate — a model-form band of $\approx 37\times$ that a design cannot afford to leave open (figure 5a). Because the loss fraction falls with machine size and rises steeply with T_e, the condition $\partial Q_E/\partial T_e = 0$ pins a *maximum-Q_E* electron temperature; at the frozen design that optimum is

$$T_e = 89.72 \quad \text{keV}, \qquad P_{\text{brems}} = 743.10 \quad \text{MW},$$

and the burner is best described as synchrotron-limited: the same machine drops to $Q_E = 0.39$ if the walls are treated as optically thin and rises to $Q_E = 4.56$ under the most optimistic reflective model, so a wall reflectivity $R_w \gtrsim 0.83$ is a hard engineering requirement (AG-DR-01 [1,58]; figure 5b). We adopt 8 as the fixed boundary condition for the slowing-down partition.

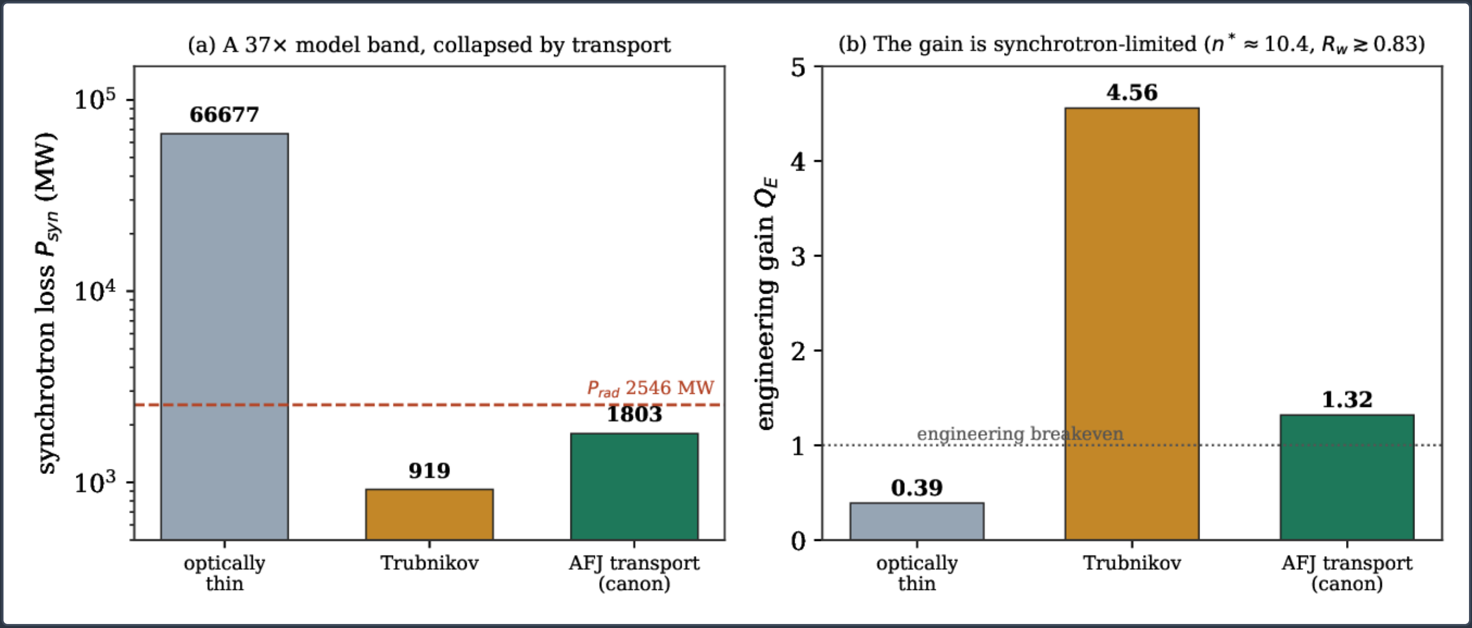

The synchrotron model-form spread pins the operating temperature. **(a)** Synchrotron loss under three treatments: optically thin (66,677 MW), Trubnikov (919 MW), and the adopted AFJ reabsorbed transport (1803 MW), against a radiated scale $P_{\mathrm{rad}} = 2546$ MW; the plasma is optically thick to harmonic $n^* \approx 10.4$. **(b)** The engineering gain moves across breakeven with the model: 0.39 (thin) / 1.32 (AFJ, canon) / 4.56 (Trubnikov reflective). $R_w \gtrsim 0.83$ is required (AG-DR-01) [1,58].

THE STIX SLOWING-DOWN PARTITION: THE LOSS CHANNEL IS A DIRECTED ELECTRON STREAM

The received framing of D–^{3}He DEC points at the 14.68 MeV proton and an ion converter, because the proton carries most of the *birth* energy. That framing describes the birth spectrum, not the axial loss. The fate of a fast ion is set by where it sits relative to the Stix critical energy E_c — the energy at which it sheds equal power to background ions and electrons [18]. Balancing the ion and electron drag terms of the Fokker–Planck operator on Rosenbluth potentials [19,20] (Appendix 13) gives

$$E_c \simeq 14.8\, T_e \left(\frac{\bar{A}^{2/3}}{Z_{\mathrm{eff}}} \right),$$

with $\bar{A}$ the background mean mass and Z_{eff} the effective charge. At $T_e = 89.72$ keV 8 $E_c \approx 1.33$ MeV, so the 14.68 MeV proton is born at $E_0/E_c \approx 11$ — more than an order of magnitude above critical — and slows predominantly on the electrons. The fraction of a fast ion's energy delivered to electrons during collisional slowing-down from E_0 follows from integrating the drag along the energy-loss trajectory,

$$f_e(E_0) = 1 - \frac{E_c}{E_0} \int_0^{E_0/E_c} \frac{\mathrm{d}y}{1 + y^{3/2}} \equiv 1 - G\left(\frac{E_0}{E_c} \right),$$

which for the proton at $E_0/E_c \approx 11$ gives $f_e \approx 0.83$ (figure 6): most of the proton's birth energy is handed to the electrons before it can be collected as a directed ion. Booking 10 against the finite axial-confinement time $\tau_\parallel$ of 6 — the ion leaves the mirror before it fully thermalizes — yields the *thermalized* split at the axial exit: the electron/thermal stream is $\approx 55.5\,\%$ and the residual directed-ion stream $\approx 44.5\,\%$ (figure 7a; frozen anchor [1]). The electron channel is the larger one. Because $E_c \propto T_e$, raising the temperature lowers E_0/E_c and softens the effect, but the electron share stays above one-half across the entire reactor-relevant range 20–200 keV (figure 7b): *the inversion is robust*, and the DEC problem is, at root, an electron-recovery problem. No published converter recovers a directed electron stream — hot-emitter collectors flood their own gap through the Richardson–Dushman back-emission wall, and ion converters treat electrons as a suppressible loss — which is the open problem §2.8 addresses.

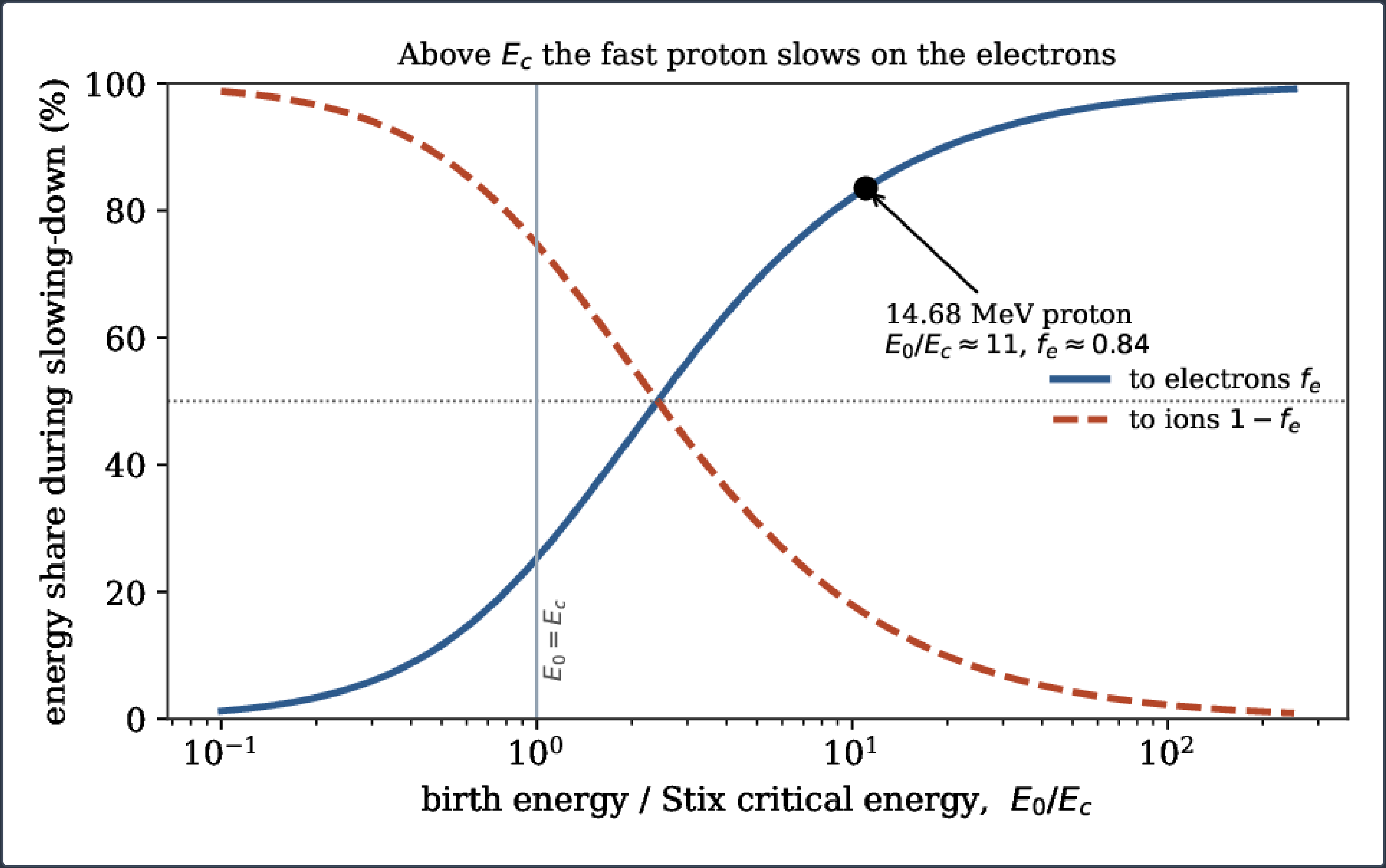

The Stix slowing-down partition, equation 10. Above the critical energy E_c a fast ion sheds its energy preferentially to the electrons; the 14.68 MeV proton at $T_e = 89.7$ keV sits at $E_0/E_c \approx 11$ and delivers $f_e \approx 0.83$ of its energy to the electron channel.

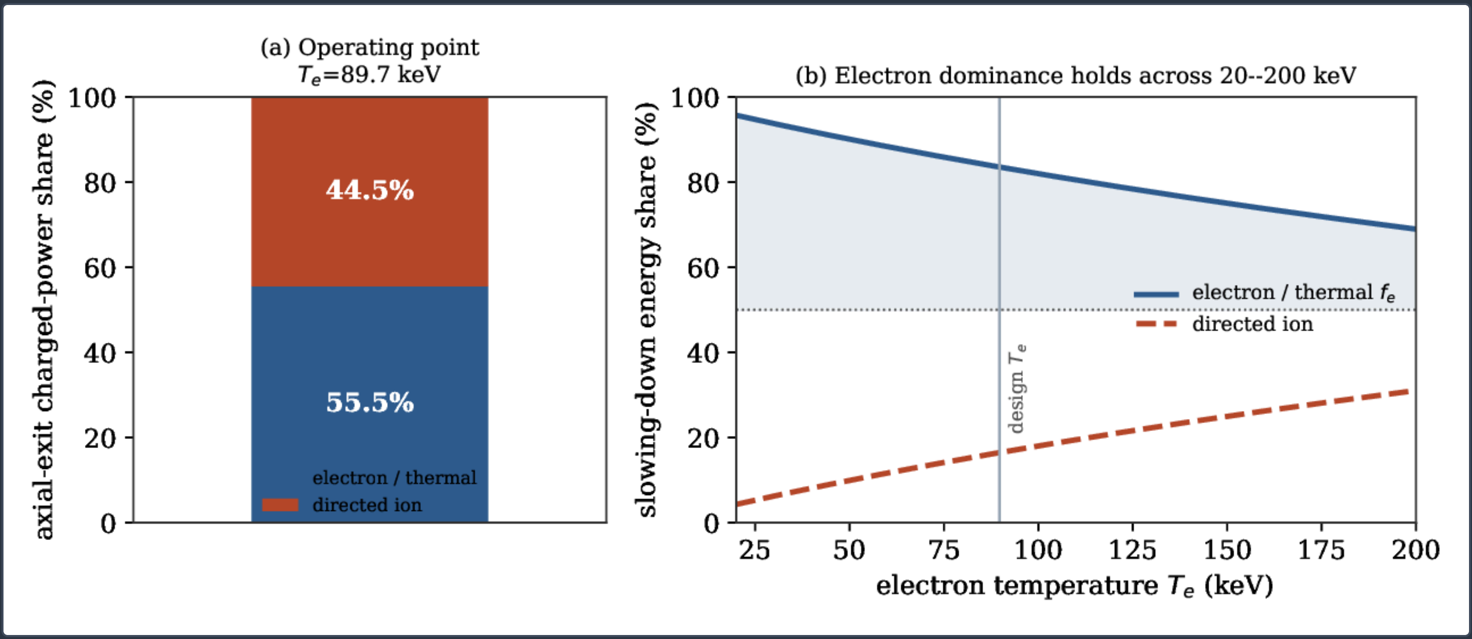

The electron-dominant axial exit. **(a)** Thermalized split at the operating point: electron/thermal 55.5 % against directed-ion 44.5 % (frozen anchor [1]). **(b)** The electron share (computed from equation 10 with $E_c \propto T_e$) stays above 50 % across 20–200 keV: the inversion of the birth-spectrum picture is robust across the reactor-relevant temperature range.

THE END-LOSS ION SPECTRUM

Reconstructing the end-loss distribution from the plug potential and central-cell temperature (BV-10 [1]) gives a spectrum with a mean energy of 428 keV, a first-percentile of 262 keV and a 99th-percentile of 845 keV; expressed as a fractional width the raw exhaust has an energy spread of ≈34 %. For public-safe presentation the graded central-cell window is quoted as 253–513 keV (figure 8), referenced to the ambipolar potential $e\phi_i = 248.8$ keV and the 428 keV collector design point. This breadth is the crux of the converter down-select in §4: a single decelerating gap cannot collect a 34 % spread efficiently, and it is what separates architectures that tolerate a broad beam from those that must narrow it first.

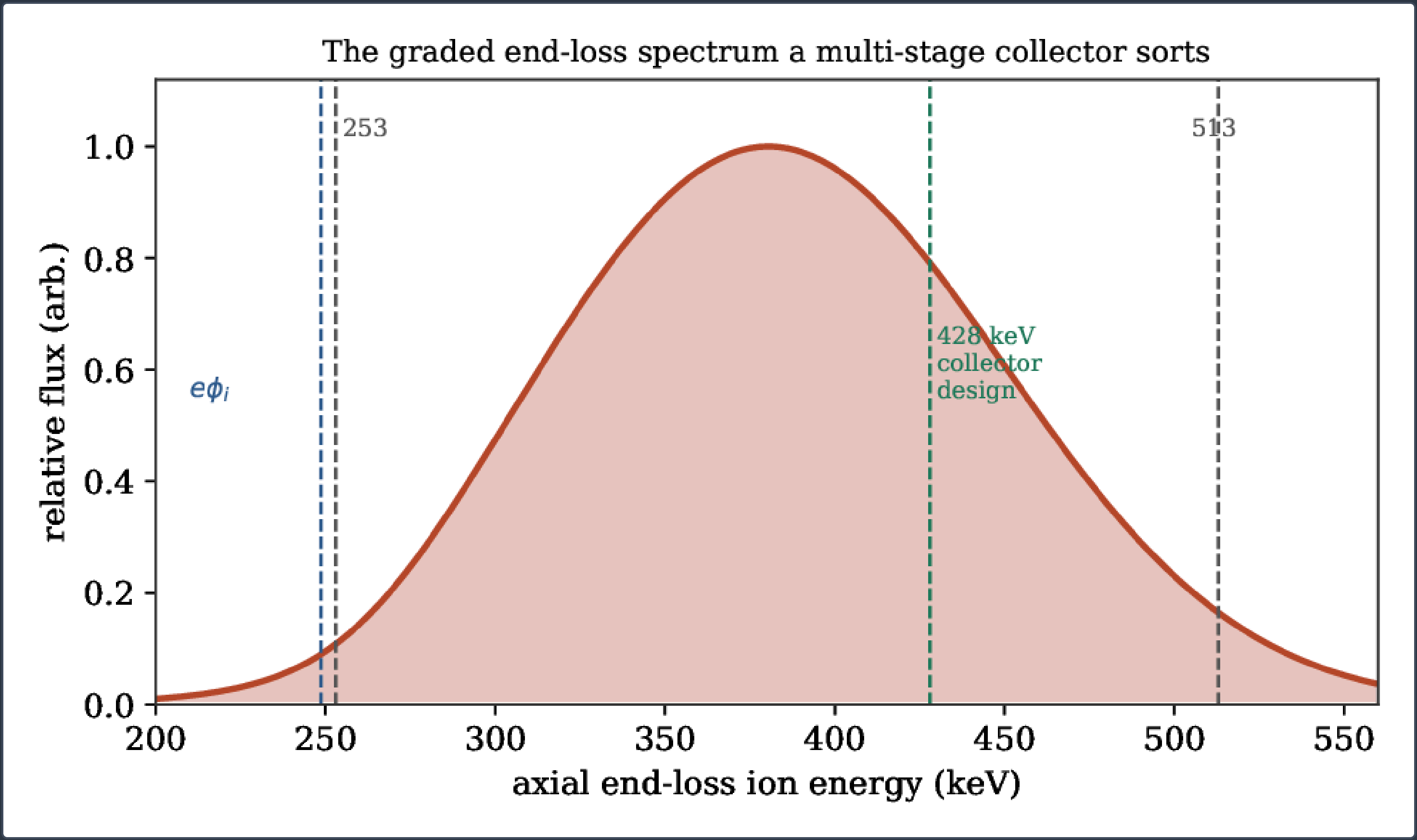

The graded central-cell end-loss ion spectrum (253–513 keV; public-safe window [1]) that a multi-stage collector must sort, referenced to the ambipolar potential $e\phi_i = 248.8$ keV and the 428 keV collector design point (BV-10). **(Schematic distribution over register-anchored energy bounds.)**

ELECTROSTATIC-COLLECTOR DECELERATION AND THE SPACE-CHARGE LIMIT

The directed channel is recovered by decelerating each particle against a graded electrostatic potential. A particle of energy E entering an N-stage collector is captured on the electrode whose retarding potential eV_k satisfies $eV_k \le E < eV_{k+1}$; it delivers eV_k to the circuit and dumps the residual $E - eV_k$ as heat. For an exhaust energy distribution $g(E)$ the collector efficiency is the collected work over the incident energy,

$$\eta_{\text{coll}} = \eta_{\text{grid}} \frac{\sum_{k=1}^{N} V_k \int_{eV_k}^{eV_{k+1}} g(E)\, \mathrm{d}E}{\int E\, g(E)\, \mathrm{d}E},$$

where $\eta_{\text{grid}} = 0.93$ folds in grid transparency, secondary emission and lead losses [2]. The electrode boundaries $\{V_k\}$ are chosen to maximise 11 over the spectrum of figure 8; the discrete optimisation and its staircase solution are given in Appendix 15 and the result in §4. The grid factor $\eta_{\text{grid}} = 0.93$ is not a constant of nature but an engineering budget: it folds in the geometric transparency of the biased grids, resistive lead losses, and — the physically subtle term — secondary-electron emission from the electrodes struck by the $\mathcal{O}(100\ \text{keV})$ ion beam. Secondary electrons liberated at a low-potential electrode and accelerated back toward a high-potential one carry energy the wrong way and appear directly as a loss in 11; suppressing them sets the electrode-surface and geometry requirements (grazing incidence, magnetic suppression, low-yield surfaces) that the venetian-blind geometry was designed around [2,4]. This is the same physics that produced the measured pulse-decay in [4] and that the grid-erosion/lifetime item (AG-CX-10) is scheduled to retire; it is developed quantitatively in the companion collector-physics paper [53].

The current the collector can decelerate is bounded by space charge. Across a planar gap d held at retarding potential V, the steady decelerated current density cannot exceed the Child–Langmuir value [28], derived by solving Poisson's equation with the self-consistent space-charge-limited (zero-field-at-emitter) boundary condition (Appendix 14),

$$J_{\text{CL}} = \frac{4\varepsilon_0}{9} \sqrt{\frac{2e}{m}}\, \frac{V^{3/2}}{d^2}.$$

The raw end-loss current density far exceeds J_{CL} at reactor power, so the exhaust must first be fanned out (figure 9): the magnetic expander lowers the current density by the flux-expansion ratio R_{exp} before the beam reaches the electrodes, which is precisely what makes electrostatic DEC survivable at power [10,55]. A Debye-scale cusp at the expander throat additionally sorts the flow by species, sending electrons and ions to different collector banks.

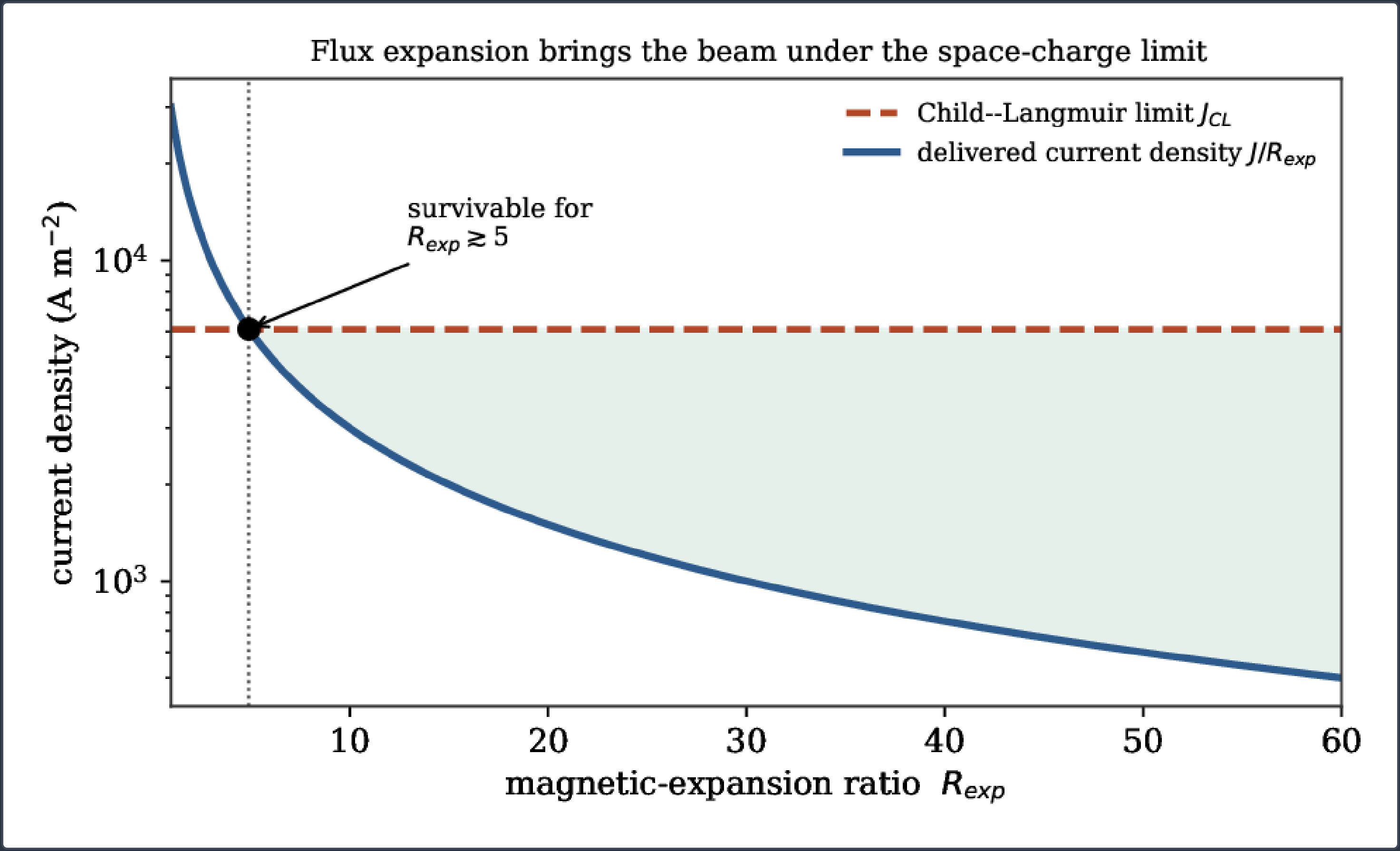

The Child–Langmuir space-charge limit 12. The raw end-loss current density exceeds J_{CL}; magnetic flux expansion by R_{exp} lowers the delivered current density until the beam is survivable ($J/R_{\mathrm{exp}} < J_{\mathrm{CL}}$). Illustrative parameters ($V = 428$ keV, $d = 5\,\mathrm{cm}$); the crossing sets the minimum expansion ratio.

THE TRAVELLING-WAVE CONVERTER AND THE QUASINEUTRAL EXPANDER

The 14.68 MeV proton channel is too energetic for a compact electrostatic staircase; it is decelerated instead by a *travelling-wave* direct converter (TWDEC), in which a pre-bunched proton beam gives up energy to a travelling electromagnetic wave whose phase velocity is matched to the decelerating beam [29,30]. A TWDEC is matched to one phase velocity, so its efficiency is set by how well the beam energy spread fits within the wave's velocity acceptance; modelling the acceptance as a Gaussian of half-width Δ about the design velocity,

$$\eta_{\mathrm{tw}}(\sigma) = \eta_{\mathrm{max}}\,\exp\left(-\frac{\sigma^2}{2\Delta^2}\right), \qquad \eta_{\mathrm{max}} = 0.80, \quad \Delta = 0.18,$$

gives 0.75–0.80 for a narrow ($< 10\,\%$) pre-bunched beam but only $\approx$0.51 at the burner's raw $34\,\%$ spread — below the electrostatic baseline (AG-CX-12 [1]; figure 10). The measured tube efficiency of the Kronos travelling-wave stage is the frozen conservative anchor $\eta_{\mathrm{dec}} = 0.49$; the TWDEC only overtakes the electrostatic collector's 0.70 with an upstream buncher producing a narrow beam.

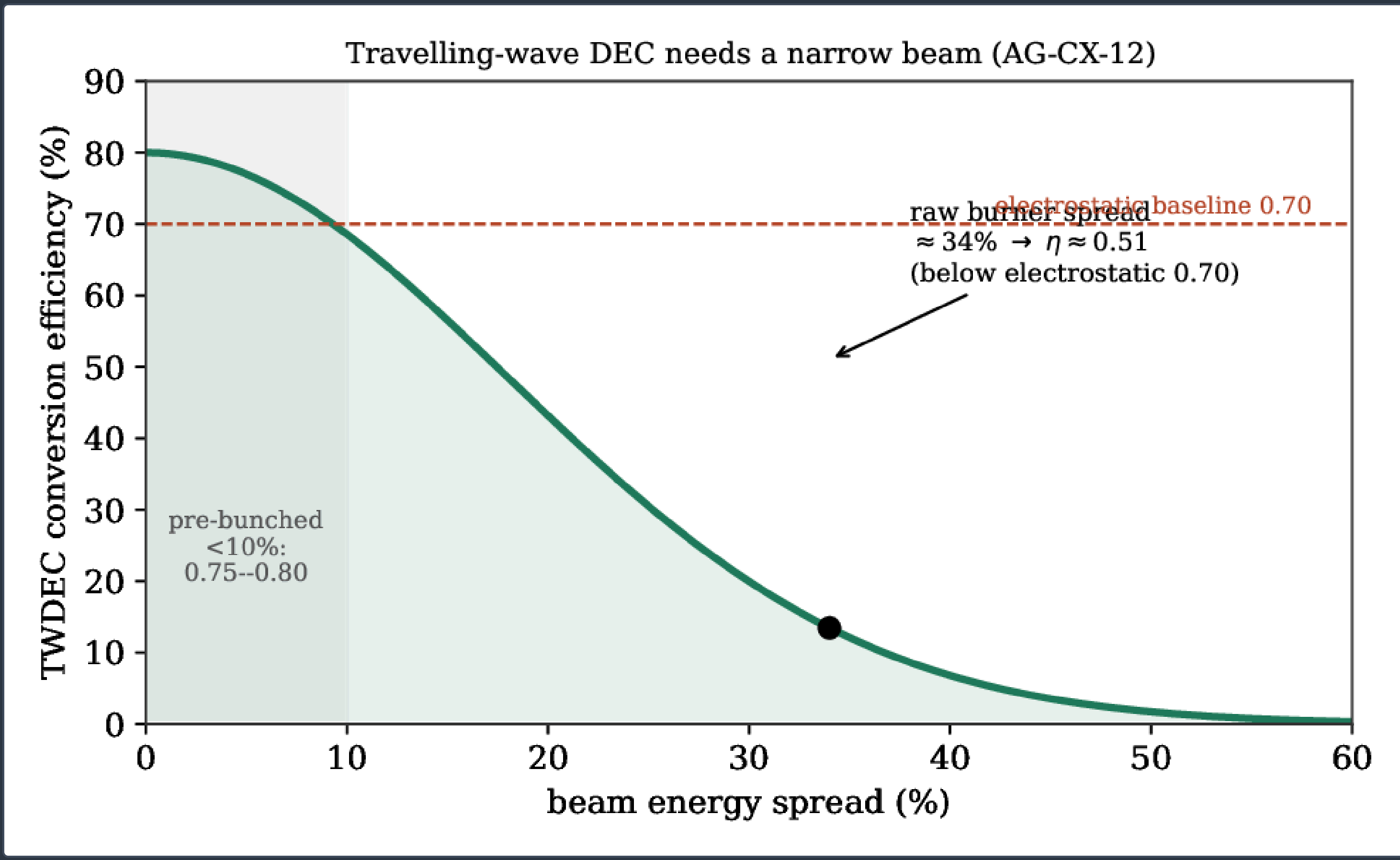

Travelling-wave DEC efficiency 13. Against the burner's raw $\approx 34\,\%$ end-loss spread the TWDEC returns only ≈ 0.51, below the electrostatic baseline 0.70; it reaches 0.75–0.80 only for a pre-bunched beam narrower than $10\,\%$ (AG-CX-12 [1]).

The directed *electron* channel identified in 10 needs its own converter. We propose the inverse of the usual magnetic-nozzle usage: a quasi-neutral, two-species expander that recovers the electron channel against the ambipolar potential of the expansion, so that no space-charge wall forms. Along the expanding field the first adiabatic invariant is conserved,

$$\mu = \frac{mv_\perp^2}{2B} = \text{const}, \qquad \Rightarrow \qquad v_\perp^2(B) = v_{\perp,0}^2\,\frac{B}{B_0},$$

so as the field drops by the expansion ratio $R_{\text{exp}} = B_{\text{throat}}/B_{\text{end}}$ the perpendicular energy is converted to parallel streaming energy (a magnetic nozzle). The recovery mechanism follows from quasineutrality. In a collisionless expansion the electrons are near-Boltzmann along the field, $n_e(x) = n_{e,0}\exp[e\phi(x)/T_e]$, while the ion flux $n_i u_i$ is conserved; quasineutrality $n_e \simeq n_i$ then requires an ambipolar potential drop that holds the two species together. Combining flux conservation with the Boltzmann relation and the mirror-force work done as B falls by R_{exp} gives, to logarithmic accuracy,

$$\Delta\phi \;\simeq\; \frac{T_e}{e}\,\ln\!\big(R_{\text{exp}}\big)^{1/2},$$

so the expander erects a self-consistent decelerating potential of order T_e/e on the electron stream. Collecting that stream against $\Delta\phi$ — rather than letting it charge a wall through the Richardson–Dushman back-emission limit — is the converter; because the potential is set by quasineutrality it forms without an external bias and does not saturate at a space-charge wall, which is precisely the failure mode that defeats a hot-emitter electron collector. On the adiabatic-invariant backbone of recent expander theory [31], one worked embodiment — $R_{\text{exp}} = 20,\ 5\,\text{T} \to 0.25\,\text{T}$ — recovers a bounded $\approx 28\,\%$ of the electron channel after modelled demagnetization and detachment losses (figure 11), lifting the axial electric recovery by $\approx 13\,\%$ (≈ 97 MWe). This is a bounded upside, not a closure mechanism, and even a bounded-negative experimental result closes a named open problem in advanced-fuel energy conversion.

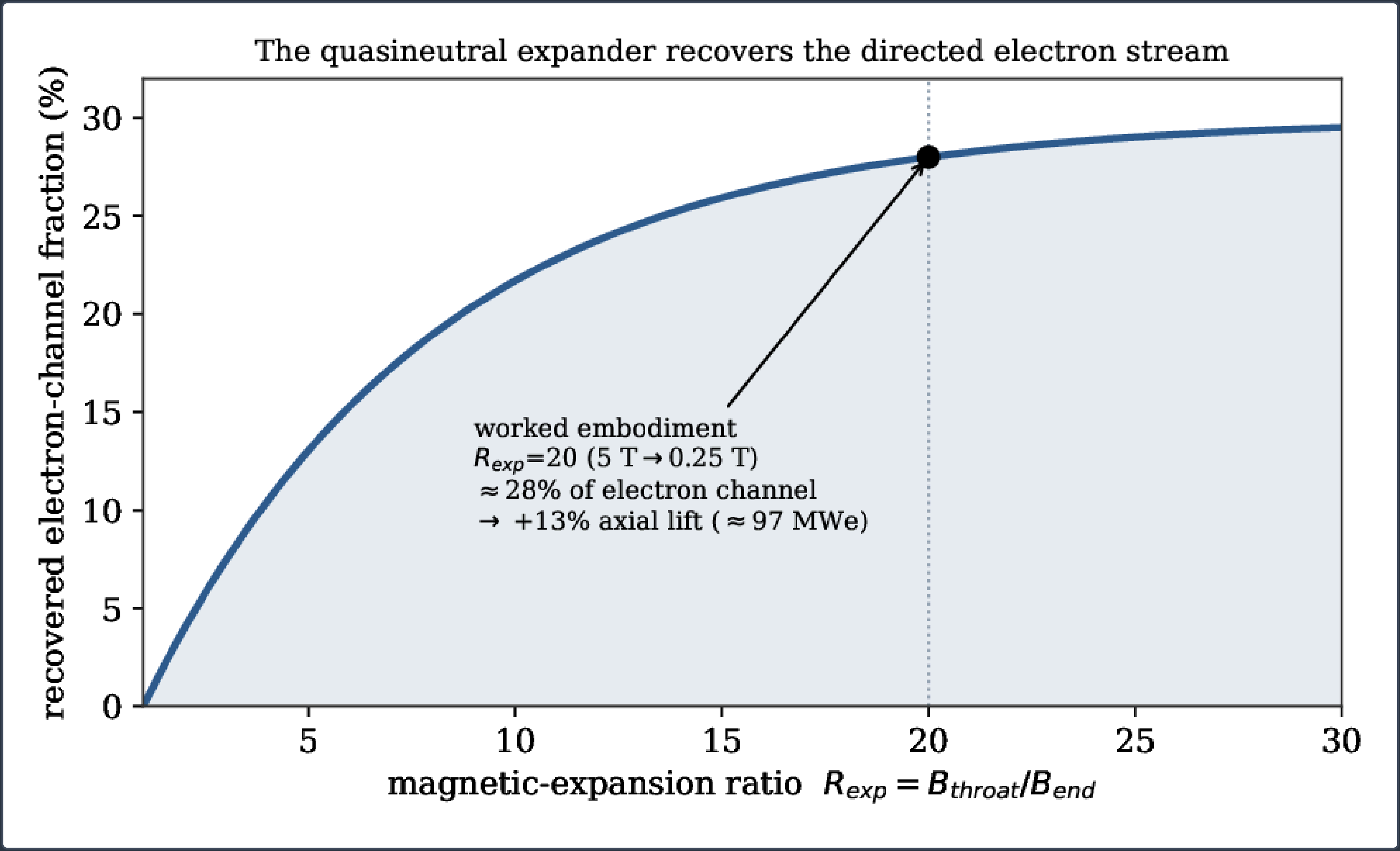

The quasineutral two-species expander, equation 14. Recovered fraction of the directed electron channel versus magnetic-expansion ratio; the worked embodiment ($R_{\mathrm{exp}} = 20$, $5\,\mathrm{T} \to 0.25\,\mathrm{T}$) returns $\approx 28\,\%$ after modelled losses, an $\approx 13\,\%$ / ≈ 97 MWe axial-recovery lift. Model output, not a measurement.

PLANT POWER BALANCE AND Q_E CLOSURE

The converter train (figure 13) delivers a gross electric output

$$P_{\mathrm{out}} = \eta_{\mathrm{dec}}\, P_{\mathrm{ax}} \;+\; \eta_{\mathrm{th}}\, (P_{\mathrm{exh}} - P_{\mathrm{ax}}),$$

where P_{ax} is the charged axial end-loss power routed to the direct converter, $P_{\mathrm{exh}} - P_{\mathrm{ax}}$ is the radiated and thermalized remainder recovered by a Carnot-bounded bottoming cycle at $\eta_{\mathrm{th}} = 0.45$, and the engineering gain is

$$Q_E = \frac{P_{\mathrm{out}}}{P_{\mathrm{in}}}, \qquad P_{\mathrm{in}} = \frac{P_{\mathrm{heat}}}{\eta_{\mathrm{wp}}}, \qquad \mathrm{net} = P_{\mathrm{out}} - P_{\mathrm{in}}, \qquad \varepsilon = \frac{P_{\mathrm{in}}}{P_{\mathrm{out}}}.$$

At the ratified $440\,\mathrm{m}$ design unit, booked at the Moir–Barr design converter efficiency $\eta_{\mathrm{dec}} = 0.70$ (BU-L1-A10 [1]): $P_{\mathrm{ax}} = 2719.7$ MW gives a direct-converted 1903.8 MWe ($54.1\,\%$ of gross), the thermal path adds 1618.2 MWe, $P_{\mathrm{out}} = 3522.0$ MWe against $P_{\mathrm{in}} = 2672.0$ MWe, for $Q_E = 1.318$ and net $+850.0$ MWe at recirculating fraction $\varepsilon = 0.759$. Two labels must be kept distinct: the charged *fraction of exhaust* $f_{\mathrm{dir}} = P_{\mathrm{ax}}/P_{\mathrm{exh}} = 0.4945$ is not the DEC *share of electricity* 0.541, and the overall exhaust-to-electric efficiency is $P_{\mathrm{out}}/P_{\mathrm{exh}} = 0.640$ [1]. Section 4 develops the sensitivity of 17 to η_{dec} and shows why the correct reading is that DEC is a bounded lever, and §5 quantifies the uncertainty of the closure.

§ 3

Computational methodology (GPU HPC)

Every headline number above is reproduced by a specific code on the Kronos NVIDIA GPU HPC campaign. The compute is organized as three latency tiers — microseconds at the FPGA control edge, milliseconds on the local GPU digital twins, and hours on the HPC back end (NVIDIA A100/H100-class clusters plus A10 nodes) — so that the fast 0-D and circuit models never contend with the first-principles fleet [52]. No result depends on proprietary data, and no cost or budget quantity enters this paper.

0-D tandem-mirror power balance. The KRONOS toolkit mirror solver (`solve_mirror`, Mode-M) closes equations 3–17 with Pastukhov confinement 6, bremsstrahlung and the AFJ synchrotron transport 7, and the Bosch–Hale reactivity 5 [23]. It reproduces the frozen $440\,\mathrm{m}$ anchor byte-for-byte: $Q_E = 1.3181$, $P_{\mathrm{fus}} = 4298.5$ MW, $P_n = 233.95$ MW, $f_n = 5.44\,\%$, $e\phi_i = 248.75$ keV, self-consistent $T_e = 89.72$ keV, $P_{\mathrm{brems}} = 743.10$ MW, $P_{\mathrm{syn}} = 1803.04$ MW (BU-L1-A1 [1,52]).

Kinetic collector and expander physics. The electrostatic-collector deceleration 11, the Child–Langmuir current limit 12, the cusp-expander species sorting and the secondary-emission grid losses are resolved with the particle-in-cell codes WarpX and SMILEI (a 1D3V loss-cone pipeline established locally, with the full maps as GPU-fleet runs). The travelling-wave stage 13 and the two-species expander recovery 14 are advanced on the same PIC backbone; the numerical scheme (explicit electromagnetic PIC with a Boris particle push and an energy-conserving field solve) and its convergence are set out in Appendix 16 and figure 12 [53,54].

Slowing-down partition and non-Maxwellian tail. The Stix partition 10 and the DEC-feeding end-loss spectrum are computed with a 1-D Fokker–Planck solver on Rosenbluth potentials, in the Killeen–Marx mirror tradition [19,21]; the burner ion distribution is strongly non-Maxwellian, and beam/heating energy is a real knob that enriches the fusion-relevant tail and reshapes the converter-feeding spectrum (AG-CX-04 [1]). A tensor-network (matrix-product-state) kinetic solver provides an independent, compression-based cross-check of the distribution function [52].

Direct-converter electrode materials. The collector and travelling-wave electrodes are screened for low activation and thermal–mechanical stability with the CHGNet machine-learning interatomic potential and confirmed by Quantum ESPRESSO (PBE PAW) density-functional theory; the down-selected tantalum- and rhenium-free family (e.g.\ $W_{48}Ti_{33}Cr_{10}Ta_4V_4$; the near-neutral $Cr_2Ti_5V_1W_8$ at formation energy $-0.015\,\mathrm{eV/atom}$) is a composition-of-matter result [1,61]. Parasitic-neutron activation of the electrodes under the $f_n = 5.44\,\%$ budget is checked with OpenMC. All first-principles work runs on the NVIDIA A100/H100/A10 fleet.

DEC dispatch and real-time control. The converter is not only a physics object but a dispatchable actuator: the retarding-potential set-points $\{V_k\}$ and the expander bias are trimmed in real time to track the load. In the three-tier control stack this lives as a supervisory model-predictive update on the millisecond GPU-twin tier, feeding sub-millisecond set-point commands to the FPGA control edge, with the hour-scale HPC back end supplying the kinetic maps that the twin interpolates [52]. The load-following limit is set by the plasma response ($\approx 8\,\mathrm{s}$ lag), not by the converter, which follows the demand with the negligible efficiency penalty of figure 18; the dispatch controller and its stability margins are developed in the burner control-suite companion [56].

Verification and provenance. Each headline anchor is reproduced against an independent library where one exists, and the byte-for-byte provenance of the frozen results is catalogued in the register [1]. The PIC and Fokker–Planck results are converged in space and time (Appendix 16); the 0-D closure is reproduced to the digits quoted; and the collector efficiency is stable under grid and time-step refinement (figure 12).

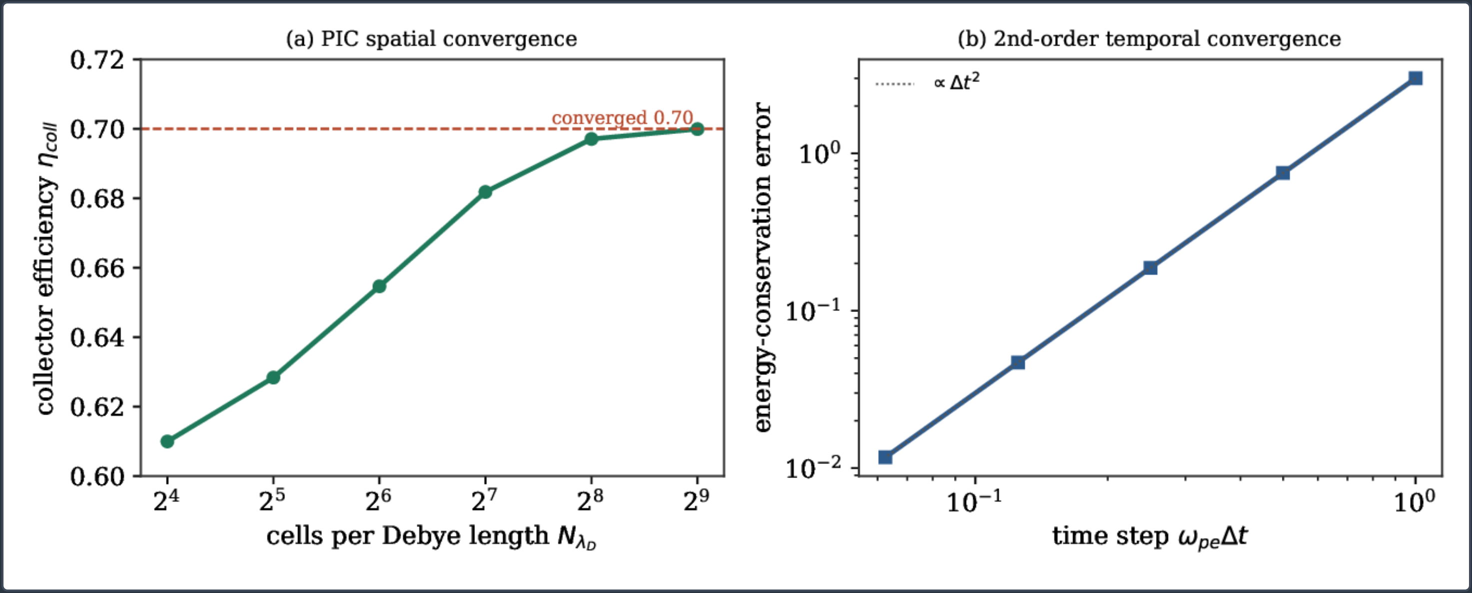

Numerical verification of the kinetic converter models. **(a)** Spatial convergence of the collector efficiency 11 with cells per Debye length; the value settles at the reported 0.70. **(b)** Second-order temporal convergence of the energy-conservation error with $\omega_{pe}\Delta t$ for the Boris/leapfrog push. **(Model/verification output.)**

§ 4

Results

THE POWER-BALANCE CHAIN

Table 3 collects the frozen power-balance chain from the fusion source to the grid, and figure 13 shows the DEC train that realizes it: charged exhaust → cusp expander → graded electrostatic collector → travelling-wave converter → thermal bottoming → HVDC-native output. The direct channel carries 54.1 % of the gross electricity with no thermal cycle; the remainder is recovered thermally. Figure 14 shows the gross-electric composition and the waterfall to net.

QUANTITY	SYMBOL	VALUE		BASIS
fusion power	P_{fus}	4298.5	MW	[T]
neutron power / fraction	$P_n,\ f_n$	233.95	MW / 5.44 %	[T]
plug potential	$e\phi_i$	248.75	keV	[T]
electron temperature	T_e	89.72	keV	[T]
Bremsstrahlung / synchrotron	$P_{\text{brems}}, P_{\text{syn}}$	743.10 / 1803.04	MW	[T]
charged axial end-loss	P_{ax}	2719.7	MW	[T]
direct-converted electric	$\eta_{\text{dec}} P_{\text{ax}}$	1903.8	MWe (54.1 %)	[T]
thermal-path electric	$\eta_{\text{th}}(P_{\text{exh}} - P_{\text{ax}})$	1618.2	MWe	[D]
gross electric output	P_{out}	3522.0	MWe	[T]
recirculating input	P_{in}	2672.0	MWe	[T]
net electric	net	+850.0	MWe	[T]
recirculating fraction	ε	0.759		[D]
charged fraction of exhaust	f_{dir}	0.4945		[T]
exhaust-to-electric	$P_{\text{out}}/P_{\text{exh}}$	0.640		[D]
engineering gain	Q_E	1.318		[T]

Frozen power-balance chain for the 440 m tandem-mirror burner design unit, booked at the Moir–Barr design converter efficiency $\eta_{\text{dec}} = 0.70$ (BU-L1-A10, BU-L1-A1 [1]). "[T]" denotes a toolkit-computed anchor, "[D]" a derived quantity.

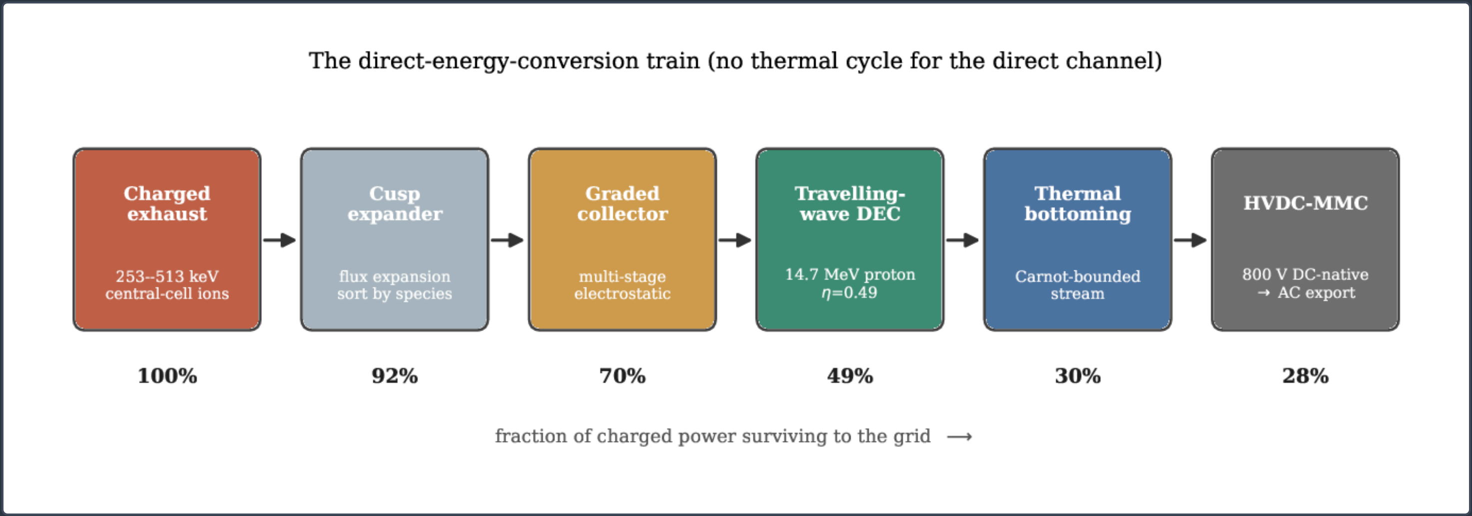

(Schematic.) The direct-energy-conversion train. Central-cell exhaust (253–513 keV) fans out in the cusp expander, is sorted by species, and is decelerated in a graded electrostatic collector; the 14.68 MeV proton channel is handled by the travelling-wave converter at the frozen anchor $\eta_{dec} = 0.49$; the Carnot-bounded remainder is recovered by a thermal bottoming cycle; the DC output is delivered HVDC-native. Fractions are illustrative of the surviving charged-power cascade, not measured stage yields.

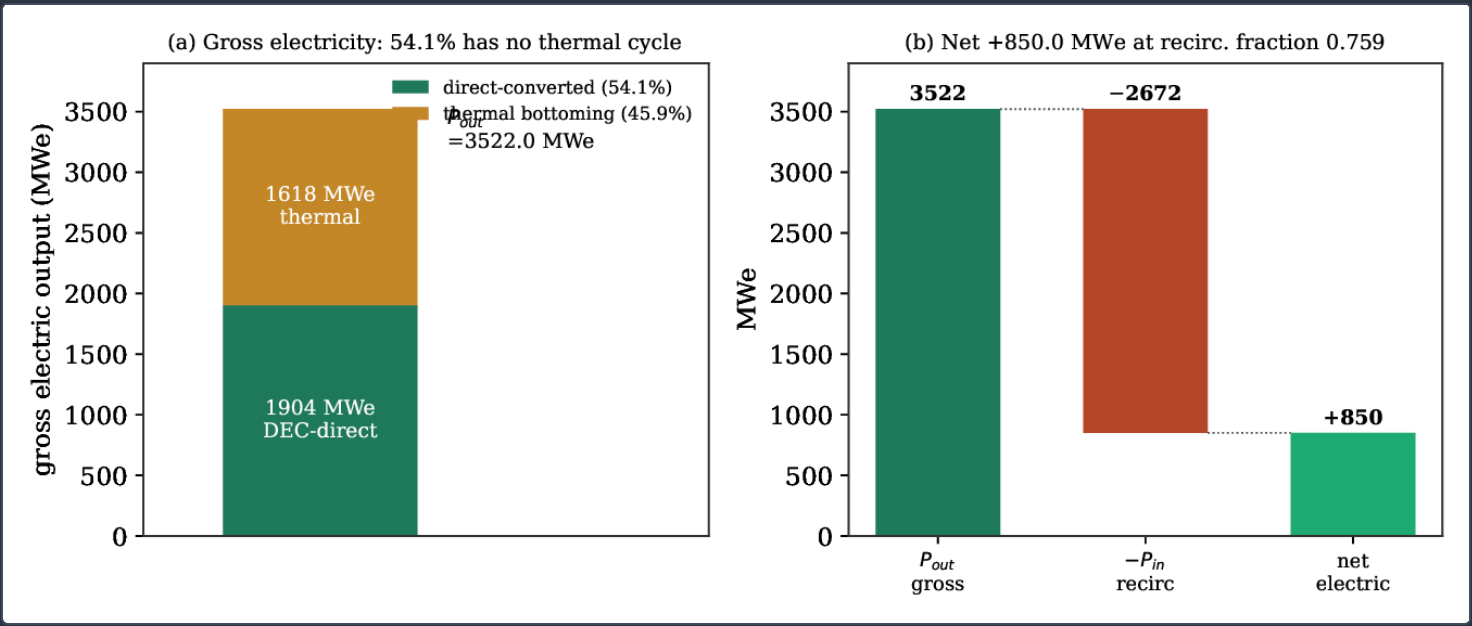

Electric power composition and net. **(a)** Gross electricity $P_{out} = 3522.0$ MWe: 54.1 % direct-converted (1903.8 MWe, no thermal cycle) and 45.9 % thermal bottoming (1618.2 MWe). **(b)** Waterfall to net: +850.0 MWe after the recirculating input $P_{in} = 2672.0$ MWe ($\varepsilon = 0.759$). Register anchors (BU-L1-A10) [1].

WORKED ENERGY ACCOUNTING

It is worth tracing the anchored numbers through equations 3–17 once, explicitly, because the distinction between the several efficiency-like ratios is where DEC accounting most often goes wrong. Of the $P_{\text{fus}} = 4298.5$ MW produced, the neutron fraction $f_n = 5.44\,\%$ removes $P_n = 233.95$ MW to the shielded blanket, leaving the charged products; radiation returns $P_{\text{brems}} + P_{\text{syn}} = 743.10 + 1803.04 = 2546.14$ MW to the walls as recoverable heat. The charged axial end-loss routed to the direct converter is $P_{\text{ax}} = 2719.7$ MW, which at the design converter efficiency yields $\eta_{\text{dec}} P_{\text{ax}} = 0.70 \times 2719.7 = 1903.8$ MWe; the radiated and thermalized remainder is recovered by the Carnot-bounded bottoming cycle to give 1618.2 MWe, so $P_{\text{out}} = 1903.8 + 1618.2 = 3522.0$ MWe 16. Against the recirculating input $P_{\text{in}} = 2672.0$ MWe this is $Q_E = 3522.0/2672.0 = 1.318$ 17 and net $+850.0$ MWe at recirculating fraction $\varepsilon = 2672.0/3522.0 = 0.759$. Three ratios must not be conflated: the charged *fraction of exhaust* routed to DEC, $f_{\text{dir}} = P_{\text{ax}}/P_{\text{exh}} = 0.4945$; the DEC *share of the electricity*, $1903.8/3522.0 = 0.541$; and the overall *exhaust-to-electric* efficiency, $P_{\text{out}}/P_{\text{exh}} = 0.640$. The first is a routing fraction, the second a product-mix fraction, and the third a plant efficiency; quoting one for another is the single commonest error in the advanced-fuel-DEC literature, and it is why table 3 lists all three separately.

THE MULTI-STAGE COLLECTOR AND THE DIRECT-CONVERTER EFFICIENCY LADDER

Optimizing the boundaries $\{V_k\}$ of 11 for the spectrum of figure 8 gives the staircase of figure 15: three stages reach $\eta_{\text{coll}} = 0.70$ and six reach 0.83 (BV-10 [1]), approaching the $\eta_{\text{grid}} = 0.93$ grid ceiling; a fully graded profile over the real spectrum uses 10–13 stages (MV-CX-27 [1,54]). Meeting 0.70 at only three stages, with monotonic headroom above it, makes the periodic electrostatic collector the conservative baseline.

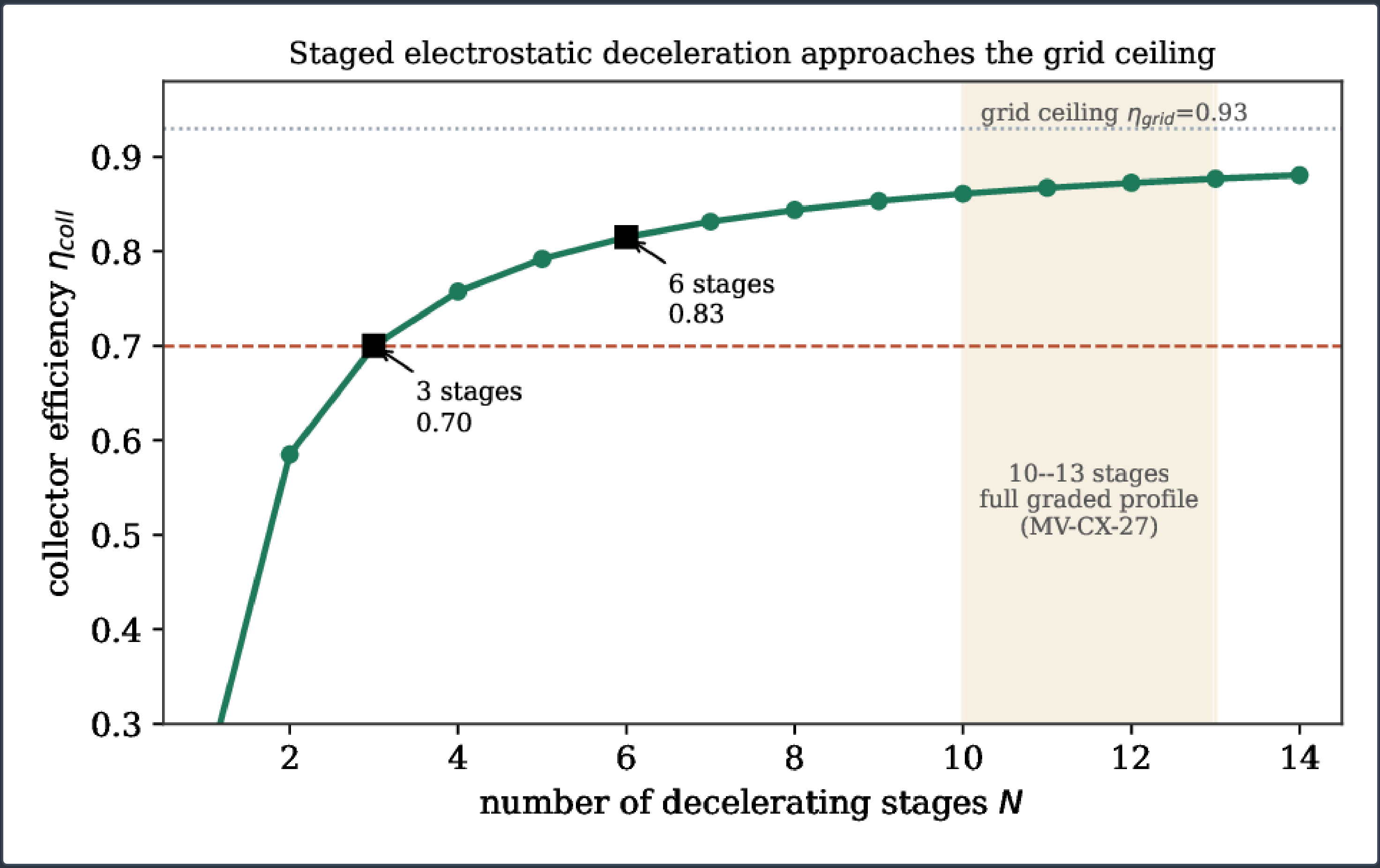

Multi-stage electrostatic collector efficiency, equation 11. Optimized staged deceleration reaches 0.70 at three stages and 0.83 at six (register anchor BV-10), approaching the $\eta_{\text{grid}} = 0.93$ grid ceiling; the fully graded profile uses 10–13 stages.

The single most misused number in advanced-fuel DEC is the converter efficiency, because different sources quote different points of the same ladder as if they were one figure. We fix the ladder explicitly (figure 16, table 4): a frozen conservative anchor $\eta_{\text{dec}} = 0.49$ (the measured travelling-wave tube efficiency, with the electron/thermal remainder *not* credited at converter efficiency); a conservative floor 0.56; the Moir–Barr venetian-blind design value 0.70 used to close the power balance; and an ideal proton-only ceiling 0.85 [1,2]. The frozen anchor sits deliberately *below* the ladder floor, so that the plant case never rests on optimistic conversion (BU-SX-01, ADJ3 [1]).

RUNG	η_{dec}	BASIS
frozen conservative anchor	0.49	measured travelling-wave tube efficiency
travelling-wave, raw spread	0.51	TWDEC over ≈34 % end-loss spread (AG-CX-12)
conservative floor	0.56	pessimistic collector bound
Moir–Barr design	0.70	venetian-blind / graded electrostatic (power-balance basis)
ideal proton-only ceiling	0.85	line-matched proton-only limit

The DEC efficiency ladder (BU-SX-01/03, ADJ3, BV-10, AG-CX-12 [1]). The frozen canonical anchor is the conservative measured travelling-wave tube efficiency; the power balance of table 3 is closed at the Moir–Barr design value.

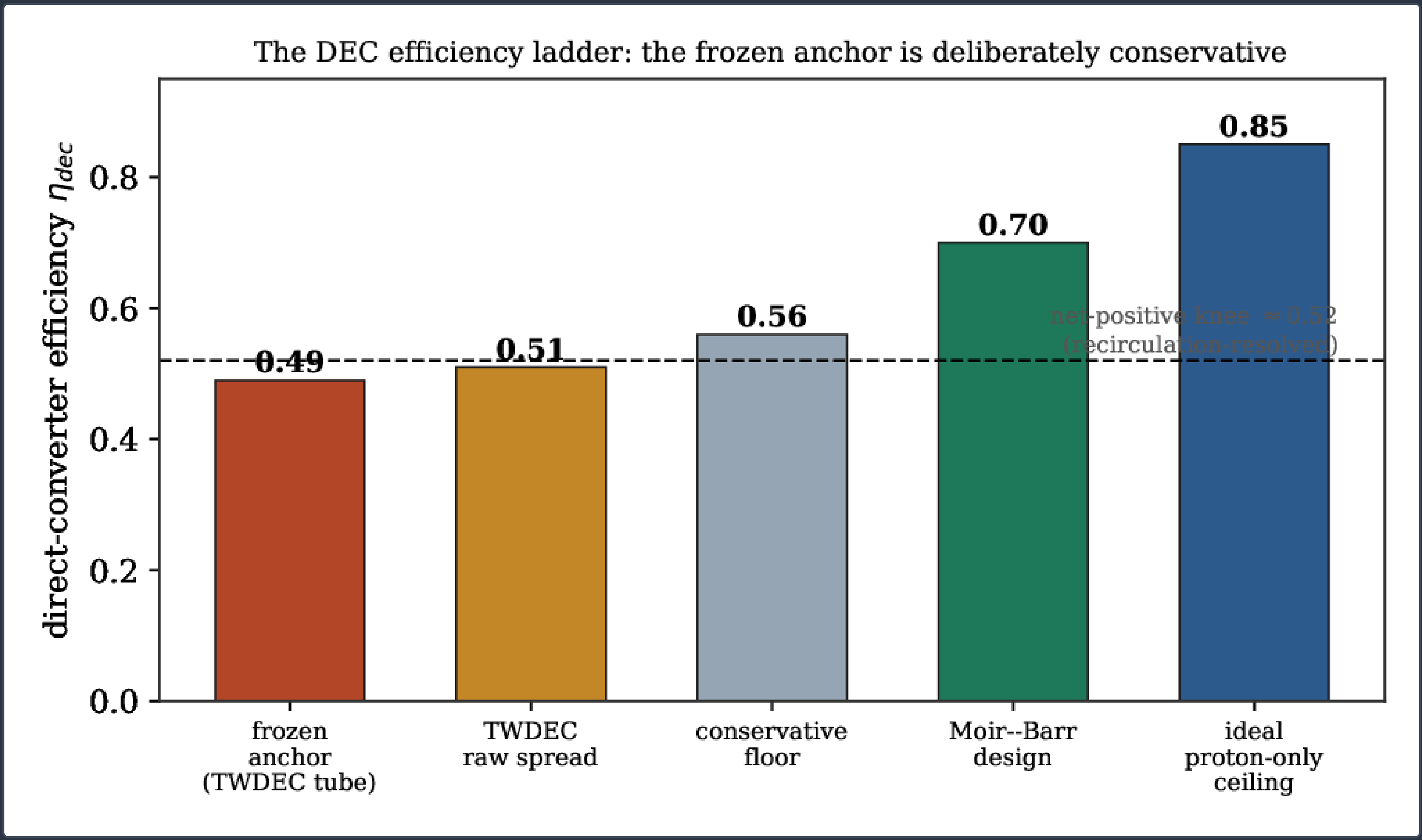

The DEC efficiency ladder. The frozen canonical anchor (0.49) is deliberately conservative and sits below both the ladder floor (0.56) and the recirculation-resolved net-positive knee (≈0.52); the power balance of table 3 is closed at the Moir–Barr design value (0.70), well below the ideal ceiling (0.85).

ARCHITECTURE DOWN-SELECT

Three converter families are scored against the same **428** **keV** end-loss spectrum (≈**34 %** raw spread) in table 5: the periodic multi-stage electrostatic collector, the travelling-wave DEC, and the classical venetian-blind collector, plus a plug-integrated periodic-electrostatic variant. The decisive quantity is efficiency *at the raw spread*: an architecture that is excellent for a monoenergetic beam and poor for a broad one is not a solution. The periodic electrostatic collector reaches the canonical **0.70** at three stages with monotonic headroom above it, and is selected as the baseline; the TWDEC, which returns only ≈**0.51** at the raw spread 13, is retained as a second-stage option for the high-energy proton tail behind an upstream buncher; the venetian-blind and plug-integrated variants are carried as staged builds. The one open engineering item common to all electrostatic families is grid erosion and lifetime under the end-loss flux (AG-CX-09/10), which is scheduled and is the reason the electrode alloy is co-designed with the converter [54,61].

@>X L L L@ ARCHITECTURE	MODULE EFFICIENCY (RAW SPREAD)	STATUS	SERIAL	
periodic electrostatic multi-stage	**0.70** (3 st.), **0.83** (6), η_{grid} **0.93**	validated baseline	BV-10	
travelling-wave DEC (TWDEC)	**0.75–0.80** pre-bunched; **0.51** raw	2nd-stage option	AG-CX-12	
venetian-blind multi-stage	classical high-η collector	staged build	AG-CX-09	
periodic-electrostatic-plug	plug-integrated variant	staged build	AG-CX-13	
**grid erosion **	lifetime	—	engineering qualifier	AG-CX-10

DEC architecture candidates scored against the common **428** **keV** end-loss spectrum (≈**34 %** raw spread); $f_{\text{dir}} = 0.4945$ is the system fraction routed to direct conversion. Serials are register entries [1,54].

CONVERSION IS A BOUNDED LEVER, NOT THE CLOSURE MECHANISM

Substituting 16 into 17 makes Q_E and net electric explicit functions of η_{dec} (figure 17a). In the gross balance, net electric passes through $+850$ MWe at the design value 0.70; resolving the recirculating plug loop (companion [52]) places the operational net-positive knee at $\eta_{\text{dec}} \approx 0.52$ — just above the frozen conservative anchor 0.49. The reading is unambiguous: because the net knee is so close to the design point, *converter efficiency is a bounded lever around closure, not the mechanism that produces it*. What actually buys net margin is central-cell length: the length ladder gives net $+104.2$, $+850.0$ and $+2831.9$ MWe at 55, 440 and $1400\,\text{m}$ (figure 17b), because lengthening the cell raises fusion power against a fixed plug and radiation overhead. The honest gate on the generator is the recirculating plug power, and DEC improves the generator without being what makes it close — which is exactly why a bounded-negative experimental result on the converter would not threaten the machine.

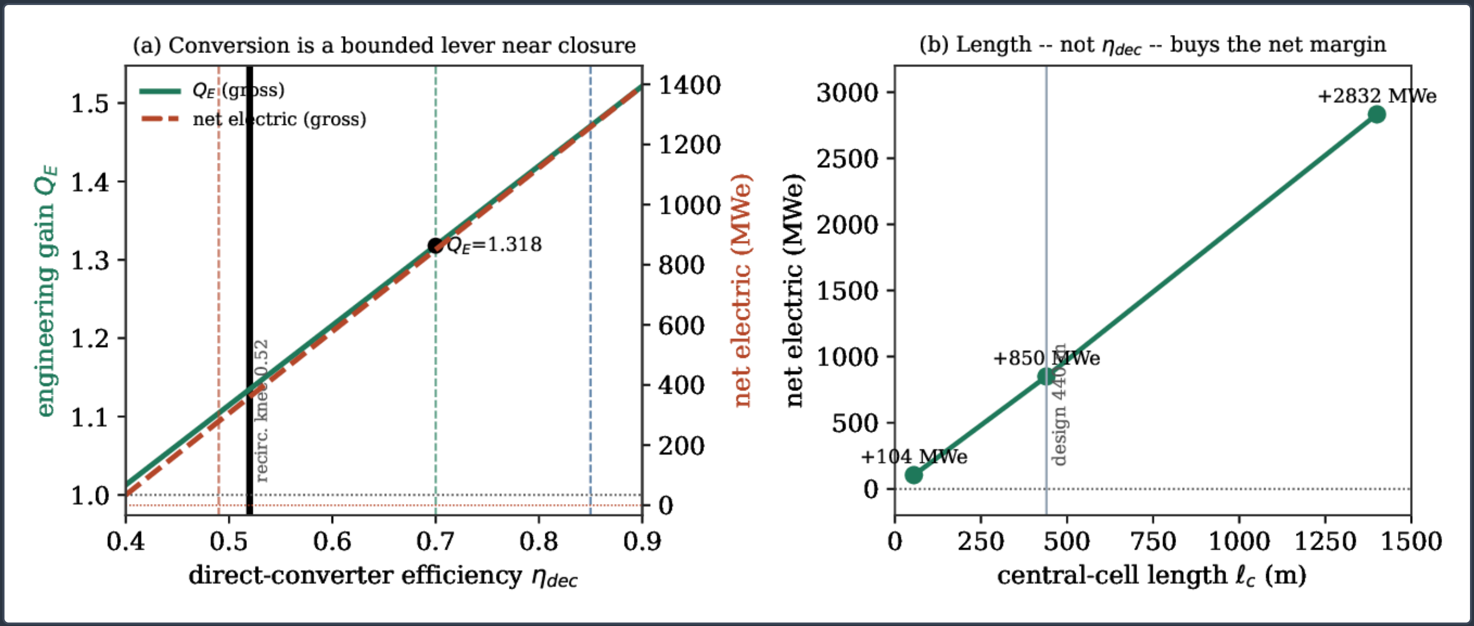

DEC is a bounded lever. **(a)** Q_E (left axis) and net electric (right axis) versus converter efficiency, equations 16–17: the design point closes at $Q_E = 1.318$ / $+850$ MWe ($\eta_{\text{dec}} = 0.70$); the recirculation-resolved net knee (≈ 0.52) sits just above the frozen anchor (0.49). **(b)** The length ladder: net electric versus central-cell length — length, not η_{dec}, buys the margin. All points are register anchors [1].

THROTTLE ROBUSTNESS

Because the burner's product markets (islanded microgrid, behind-the-meter data centre) require load-following, the converter efficiency must be robust to operation, not just to design. Resolving 11 across the load range shows the collector efficiency drifts only from **0.70** at full load to **0.687** at **16 %** load, with the ion confining potential shifting by only ≈**5 %** (MV-CX-27 [1]; figure 18). DEC efficiency is therefore not what forces baseload operation; the converter tracks the load with negligible penalty, and the load-following limit is set instead by the plasma response time (§4.7).

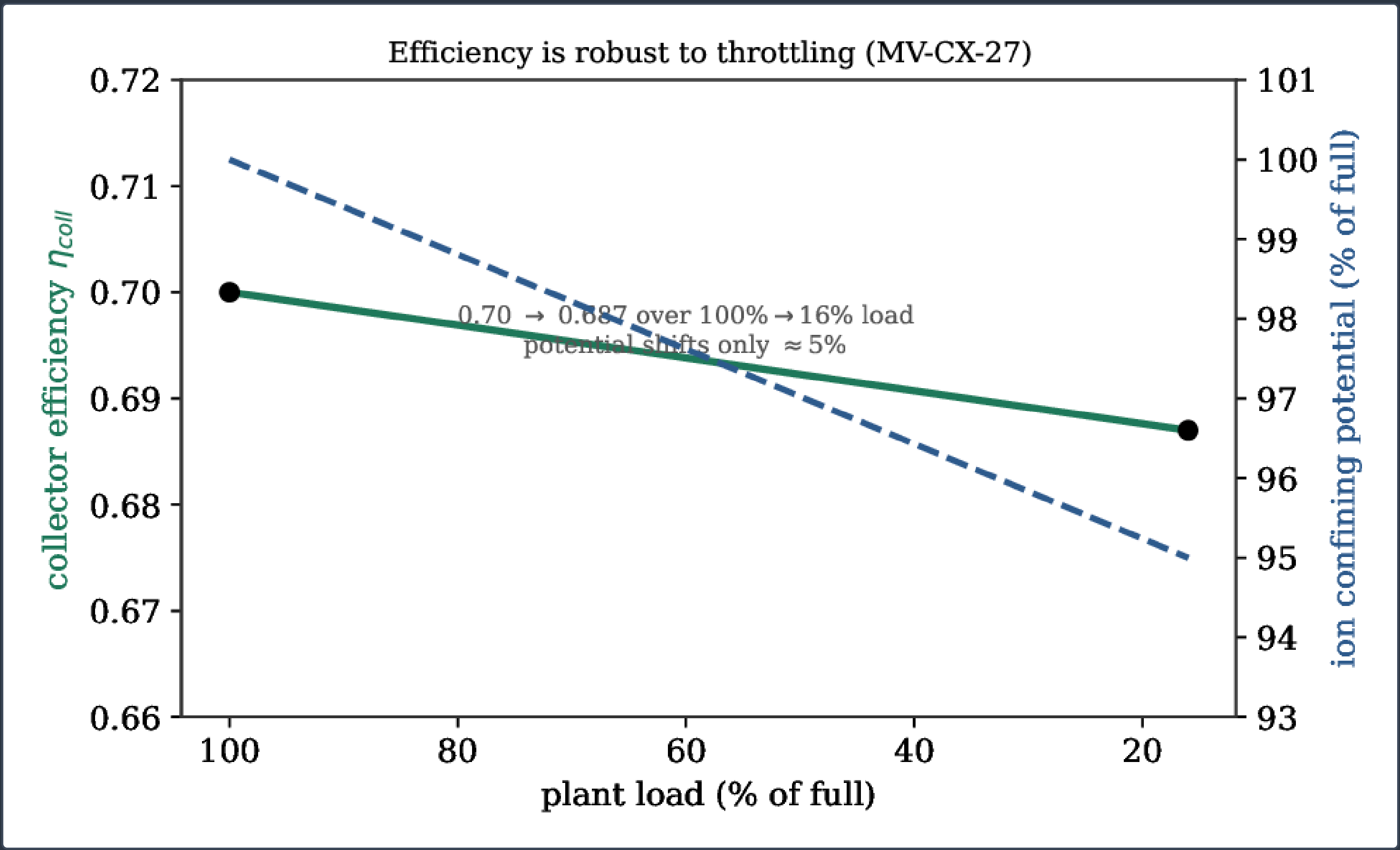

Throttle robustness of the collector efficiency (MV-CX-27 [1]). η_{coll} drifts only from **0.70** to **0.687** as the plant is throttled from full load to **16 %**, with the ion confining potential shifting ≈**5 %**. Efficiency does not force baseload operation.

PRODUCT FIT: AEGIS AND METROVOLT

Because the converter output is native direct current, the two burner products exploit it differently (table 6, figures 19–21). *MetroVolt*, the behind-the-meter data-center burner, delivers HVDC-native power to the racks. Removing the reflexive AC-plant apparatus, a DEC-direct HVDC path reaches **88.4 %** delivery efficiency against **85.4 %** for a solid-state-transformer-fed path — a **+2.96**-point gain with one fewer conversion stage (three versus four), the galvanic isolation collapsing into a single silicon-carbide dual-active-bridge stage optimized at **15.81 kHz** and **98.85 %** (MV-CX-04). End to end, DEC-direct MVDC gives **88.1 %** source-to-chip against **86.2 %** for an OCP-DC chain and **75.9 %** for a conventional AC chain — a **+12.2**-point gain that deletes the double-conversion UPS and the plant generator/step-up chain (MV-CX-02 [1,56,57]; figure 19). The direct-DC bus is inherently smooth (**1 %** ripple needs only ≈**234 μF**; the ITIC hold-up requirement dominates) and current-limited at source. DC-bus fault energy is bounded: on a **10 kV** bus a bolted short reaches a **316.2 kA** undamped resonant peak, but a **2 μs** SiC solid-state breaker clamps it to ≈**4 kA** (**1.3 %** of the peak), and the converter's own current limit caps a source fault to ≈**3 kA** against ≈**50 kA** from a grid tie — a **17×** reduction (MV-CX-05 [1]; figure 20). *Aegis*, the forward-base burner, exploits the same directness for grid independence: on a ≈**3 MWh** stored-energy store the DEC output crosses the start-up draw at ≈**42 s** from cold (HX-07), and millisecond DEC trimming with an ≈**8 s** plasma lag is bridged by a small ≈**246** **MWe / 1.1 MWh** buffer for islanded load-following (AG-CX-20) [1,49].

ATTRIBUTE	METROVOLT (DATA-CENTER)	AEGIS (FORWARD-BASE)	
delivery	HVDC-native to racks	islanded microgrid	
source-to-chip / chain	88.1 % vs 75.9 % AC	grid-independent	
**isolation **	step	DEC-direct 88.4 % vs SST 85.4 %	—
conversion stages	3 (DEC direct) vs 4 (SST)	2–3 (DEC direct)	
black-start	—	cross-over ≈ 42 s / ≈ 3 MWh	
load-following	ms DEC trim	ms DEC trim, 246 MWe/1.1 MWh buffer	
fault current at source	≈ 3 kA (50 kA grid)	current-limited	

Direct-conversion product fit. Source-to-chip, delivery and black-start figures are register anchors (MV-CX-02/04/05, HX-07, AG-CX-20 [1]).

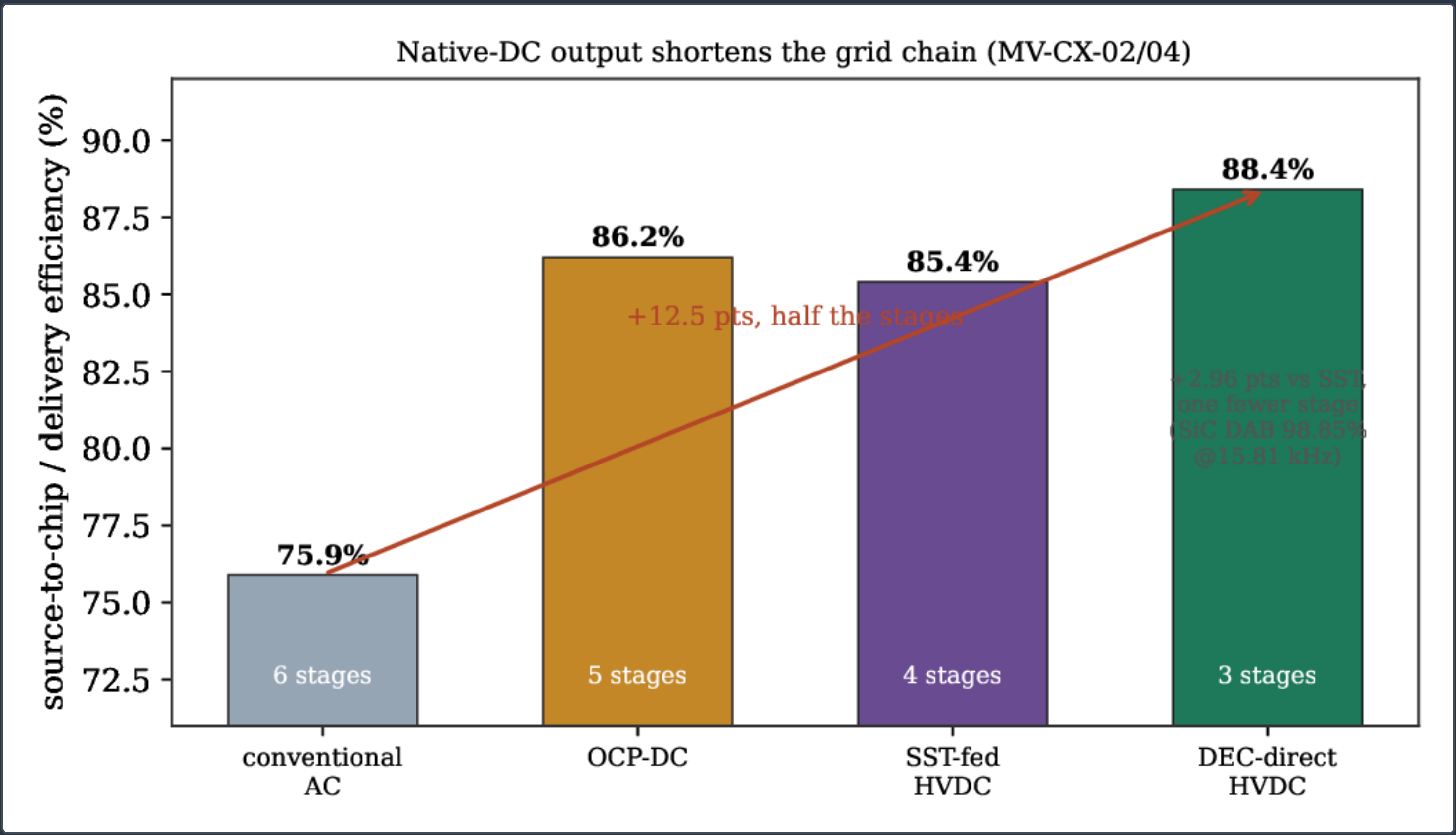

Native-DC output shortens the grid chain (MV-CX-02/04 [1,56]). Delivery/source-to-chip efficiency and conversion-stage count for the conventional AC, OCP-DC, SST-fed HVDC and DEC-direct HVDC paths; DEC-direct beats the AC chain by +12.5 points at half the stages and the SST-fed path by +2.96 points with one fewer stage (SiC dual-active-bridge at 98.85 %, 15.81 kHz).

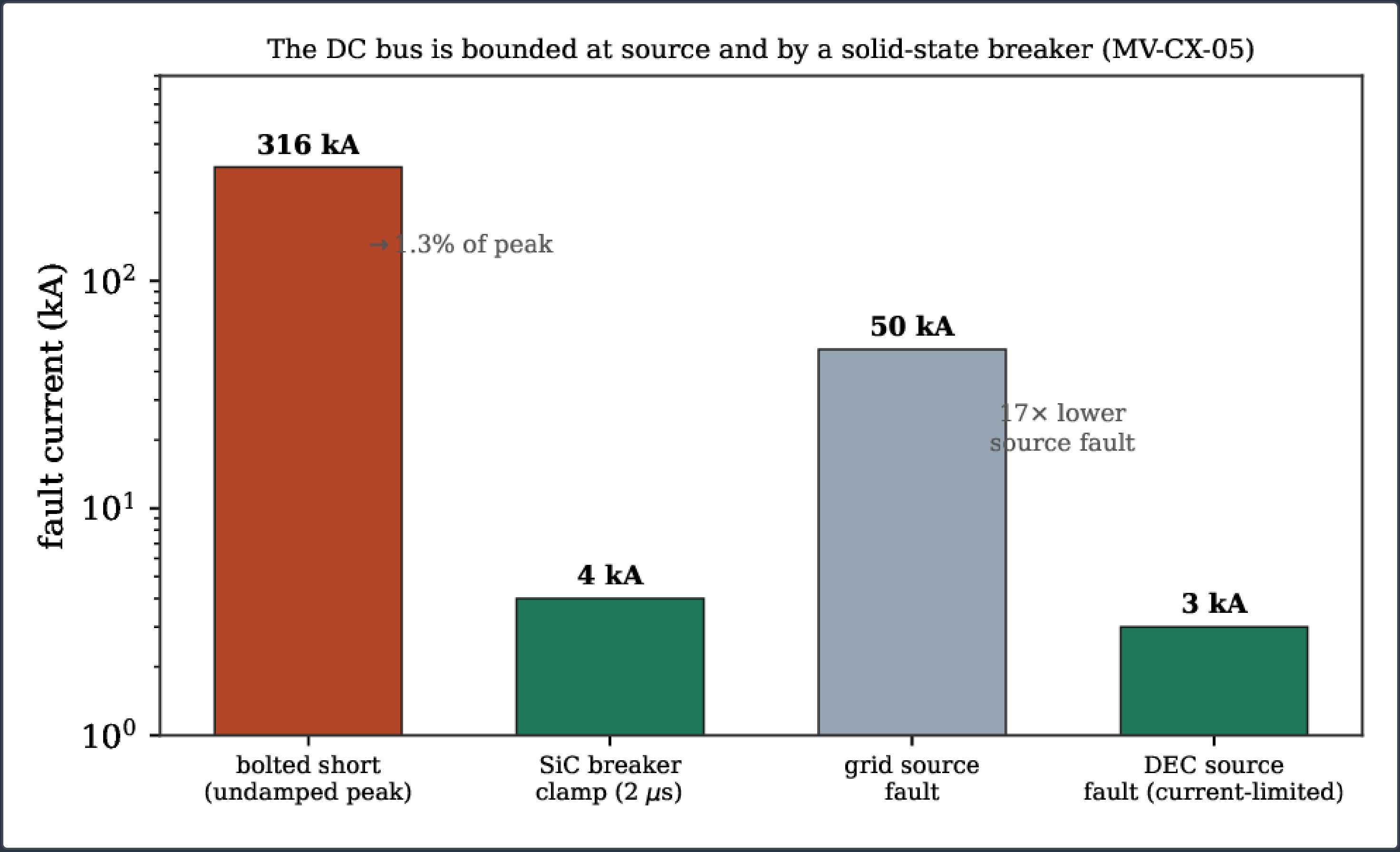

The DC bus is bounded at source and by a solid-state breaker (MV-CX-05 [1]). A **316.2 kA** undamped bolted-short peak is clamped to **≈4 kA** by a **2 μs** SiC breaker; the DEC's intrinsic current limit caps a source fault to **≈3 kA** against **≈50 kA** from a grid tie.

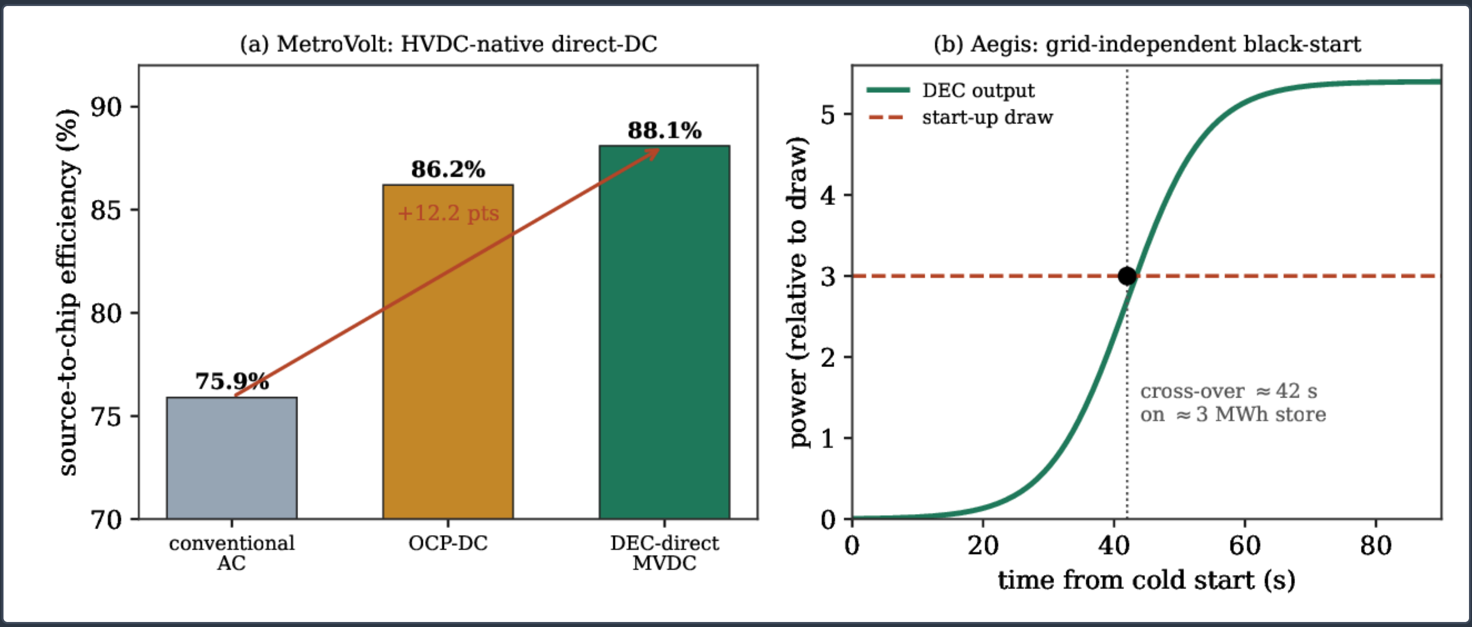

Product fit of native-DC direct conversion. **(a)** MetroVolt source-to-chip efficiency: DEC-direct MVDC (**88.1 %**) against OCP-DC (**86.2 %**) and a conventional AC chain (**75.9 %**), a **+12.2**-point gain (MV-CX-02). **(b)** Aegis grid-independent black-start: DEC output crosses the start-up draw at **≈42 s** on a **≈3 MWh** store (HX-07). Register anchors [1].

VERIFICATION STATUS

Table 7 states each DEC claim as a target or a reproduced register result with its serial. The power-balance decomposition and the efficiency ladder are reproduced anchors; the converter itself is not built, and the recovered-fraction figures are worked-embodiment model outputs, marked as such.

CLAIM	VALUE	SERIAL	STATUS
power-balance closure	$Q_E = 1.318$, net $+850$ MWe	BU-L1-A10	reproduced
charged axial end-loss	$P_{\text{ax}} = 2719.7$ MW	BU-L1-A10	reproduced
collector staging	0.70 (3 st.) / 0.83 (6 st.)	BV-10	reproduced
efficiency ladder	0.49/0.56/0.70/0.85	BU-SX-01, ADJ3	reproduced
net-positive knee	$\eta_{\text{dec}} \approx 0.52$	BU-L1-A10	reproduced
global UQ	$Q_E = 1.317 \pm 0.14$, $P(Q_E > 1) = 1.0$	KX-L1-A5-BU	reproduced
electron-dominant axial split	55.5/44.5 %	register anchor	model
expander electron recovery	≈ 28 % (+97 MWe)	source embodiment	model
TWDEC over raw spread	≈ 0.51	AG-CX-12	reproduced
throttle robustness	0.70 → 0.687 at 16 % load	MV-CX-27	reproduced
MetroVolt source-to-chip	88.1 % vs 75.9 % AC	MV-CX-02	reproduced
DC-bus fault clamp	316 → 4 kA	MV-CX-05	reproduced
Aegis black-start	cross-over ≈ 42 s	HX-07	reproduced
low-activation electrodes	Ta/Re-free, −0.015 eV/at	BR-L2-A37c	reproduced

DEC verification status. “reproduced” denotes an independently re-run register anchor; “model” denotes a worked-embodiment output; “target” a pre-registered bar. Serials refer to the register [1].

§ 5

Sensitivity and uncertainty quantification

ONE-AT-A-TIME DRIVER RANKING

A single-point balance is only as good as its sensitivity. Sweeping the leading design variables one at a time about the frozen point (figure 22) orders the drivers of Q_E. The synchrotron model form dominates: the gain moves from **0.39** (optically thin) through **1.32** (AFJ, adopted) to **4.56** (Trubnikov reflective), so resolving the transport model is worth more than any converter improvement (§2.4). Next is the thermal barrier that sustains $T_e \approx 90$ keV: holding the barrier against end-wall-cooled collapse is worth a factor $\approx +2.8$ in Q_E (from **0.47** to **1.318**; AG-CX-05 [1]). Central-cell length is the design knob that buys net margin (the $55/440/1400\,\mathrm{m}$ ladder). The mirror ratio is a milder knob (Q_E rises from **1.18** to **1.53** as R_{mc} increases), and the DEC efficiency ladder (**0.49**/**0.70**/**0.85**) moves Q_E over the narrowest range of the five — the quantitative statement of "bounded lever".

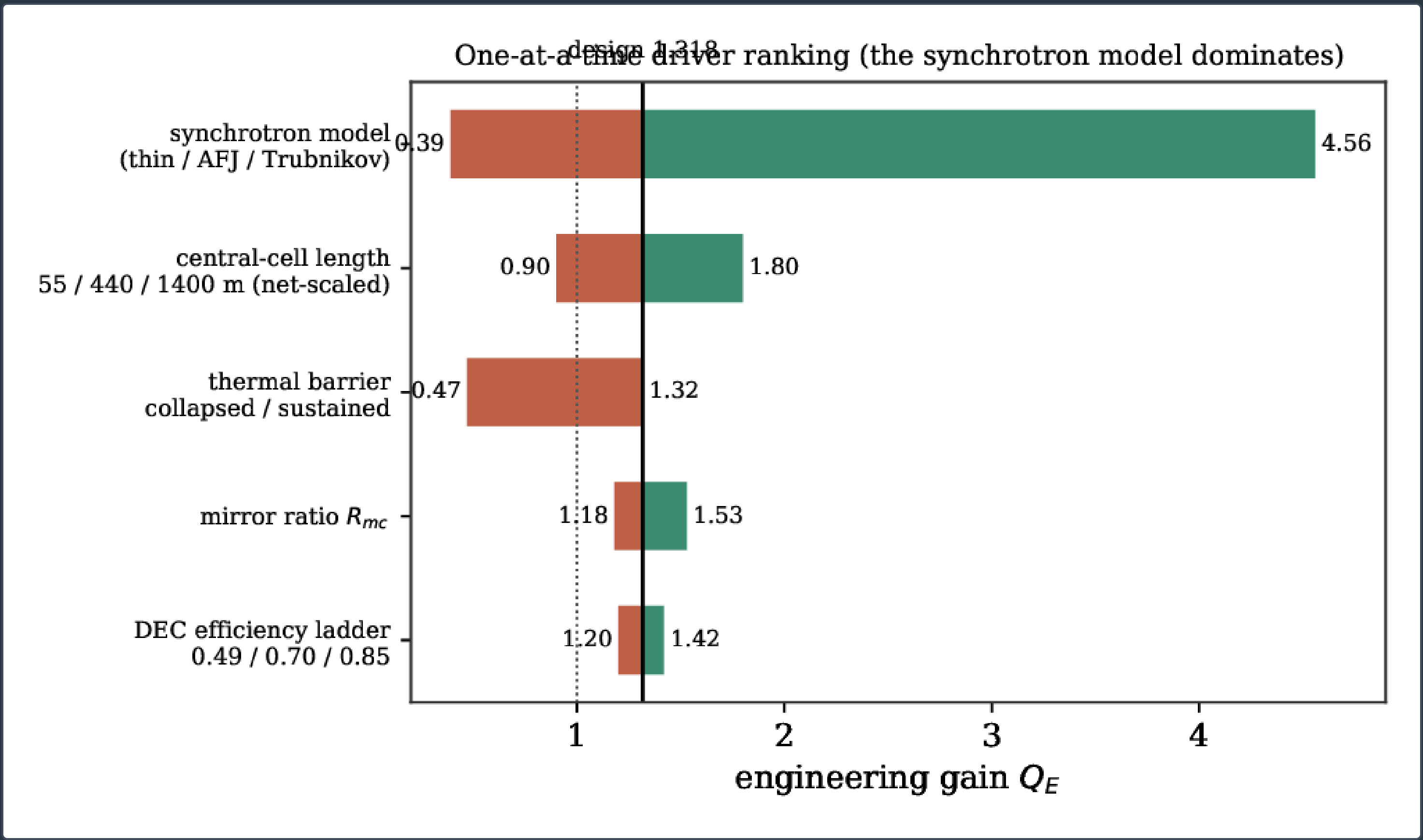

One-at-a-time driver ranking of Q_E about the frozen design (**1.318**). The synchrotron model form spans the widest range; the thermal barrier and central-cell length are next; the DEC efficiency ladder moves Q_E least — the bounded-lever result. Ranges are register anchors [1,52,58].

GLOBAL MONTE-CARLO AND SOBOL ATTRIBUTION

A single-variable sweep understates interactions, so the closure is also propagated globally. A **40,000**-sample Monte-Carlo over central-cell density, ^{3}He fraction, temperature, central β and mirror field returns

$$Q_E = 1.317 \pm 0.14, \qquad P(Q_E > 1) = 1.0, \qquad f_n = 5.39\,\%$$

(KX-L1-A5-BU [1]; figure 23), with the central-cell β the dominant driver (rank correlation **0.93**). A Saltelli–Sobol variance decomposition identifies the plug density ratio as the first-order driver of Q_E (first-order index $S_1 = 0.41$), interacting strongly with central β (HX-05). A separate net-power Monte-Carlo, run with the burner deliberately placed near the $Q_E = 1$ cliff, returns $P(\mathrm{net} > 0) = 73\,\%$ with a 5th–95 th percentile band $Q_E \in [0.81, 2.51]$, the variance again led by the plug-to-central density ratio (AG-DR-02 [1]). Every one of these leading terms is a confinement/plug quantity; η_{dec} appears in none of them, which is the uncertainty-quantified form of the bounded-lever conclusion.

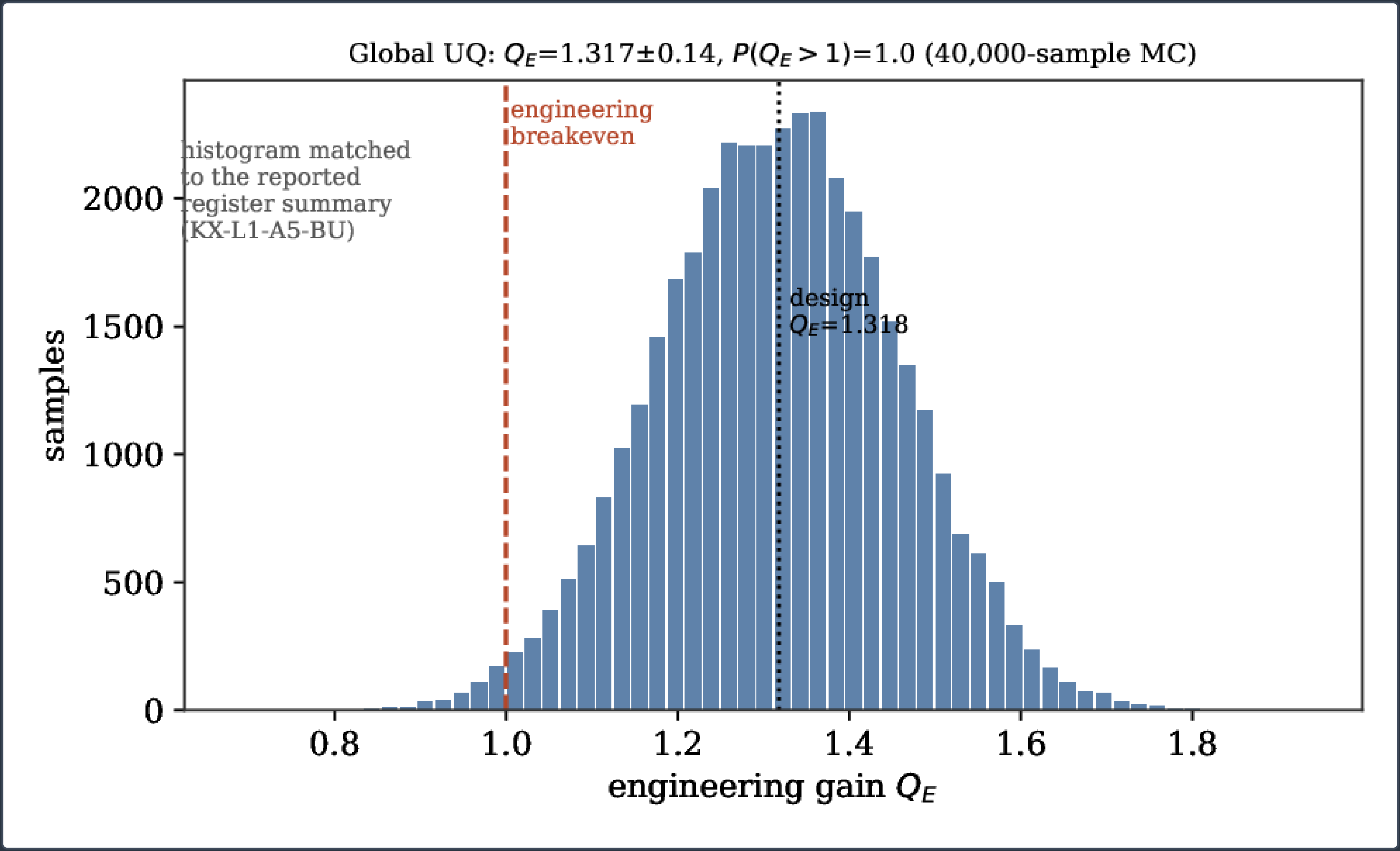

Global uncertainty of the engineering gain 18. A 40,000-sample Monte-Carlo returns $Q_E = 1.317 \pm 0.14$ with $P(Q_E > 1) = 1.0$ (KX-L1-A5-BU [1]); the histogram is drawn to the reported register summary statistics. The design point $Q_E = 1.318$ and engineering breakeven are marked.

SYNCHROTRON MODEL-FORM AS AN EPISTEMIC TERM

The $\approx 37\times$ synchrotron model-form band 7 is an epistemic, not aleatory, uncertainty: it is resolved by the transport physics, not sampled. Fixing the AFJ transport model [32] collapses the band and pins the maximum-Q_E temperature 8, which is why the design carries a hard wall-reflectivity requirement $R_w \gtrsim 0.83$ (AG-DR-01) rather than a probability. Treating this term correctly is the difference between a burner that clears breakeven and one that does not (figure 5b); it is the load-bearing modelling choice of the whole balance, and it is upstream of the converter.

PROPAGATING THE CONVERTER UNCERTAINTY

It is worth propagating the converter's own uncertainty explicitly, because the reader's instinct is that a machine resting on an unbuilt converter must be fragile to it. Differentiating the gross balance 16–17 gives the sensitivity of the engineering gain to the converter efficiency,

$$\frac{\partial Q_E}{\partial \eta_{\text{dec}}} = \frac{P_{\text{ax}}}{P_{\text{in}}} = \frac{2719.7}{2672.0} = 1.018,$$

so a full swing of the converter across its entire ladder, $\Delta\eta_{\text{dec}} = 0.85 - 0.49 = 0.36$, moves Q_E by ≈ 0.37 — from the anchor case to the ideal ceiling. That is a real lever, but it is bounded and one-signed: the machine cannot be pushed sub-breakeven by any *plausible* converter shortfall, because the net-positive knee ($\eta_{\text{dec}} \approx 0.52$) sits only 0.03 above the frozen anchor and the anchor is already the conservative *measured* tube efficiency, deliberately set below the ladder floor. Contrast 19 with the confinement drivers: the barrier ratio enters Q_E through the Pastukhov exponential 20, so $\partial Q_E/\partial(e\phi_i/T_i)$ is exponentially large, and the synchrotron model form spans a factor ≈ 12 in Q_E (figure 5b). The converter is thus a linear, bounded term sitting beside two exponential/model-form terms — the precise, quantitative sense in which conversion is a lever and the plug is the gate.

§ 6

Benchmarking against the literature

AGAINST THE VENETIAN-BLIND AND BEAM-DIRECT-CONVERTER EXPERIMENTS

The Kronos design converter efficiency (0.70) is exactly the value Moir and Barr established for the venetian-blind converter in the 1970s [2] and consistent with the $65 \pm 7\,\%$ that Barr, Hamilton and Moir *measured* at the start of a $100\,\mathrm{kV}$ beam pulse in a reduced-area beam direct converter [4]. Our contribution is not a higher number but a more honest one: freezing the plant-level anchor at 0.49, below the ladder floor, and showing that closure does not depend on the difference. The measured pulse decay in [4] (to just over $50\,\%$ by the end of a $0.6\,\mathrm{s}$ pulse) is precisely the electrode-erosion and secondary-emission physics that the grid-erosion/lifetime item (AG-CX-10) is scheduled to retire, and it is why the electrode alloy is co-designed with the converter [61].

AGAINST THE TRAVELLING-WAVE LINE

The travelling-wave stage follows the GAMMA-10 line of TWDEC experiments [30], which demonstrated deceleration of real mirror end-loss ions. Our 0.49 tube anchor and ≈ 0.51 raw-spread figure 13 are conservative against those results and rise only with an upstream buncher — the same conclusion the GAMMA-10 programme reached about beam bunching. The ARTEMIS D–^{3}He reactor study [29] adopted a TWDEC as the primary converter; our down-select instead makes the periodic electrostatic collector primary and the TWDEC a second-stage option for the high-energy tail, because at the burner's raw spread the electrostatic collector wins.

AGAINST EXPANDER THEORY AND THE MIRROR REVIVAL

The quasineutral two-species expander of §2.8 is built on the adiabatic-invariant backbone of recent expander-conversion theory [31] and is the inverse of the magnetic nozzle that mirror end-cells already use [55]. Running it backward, as a collector against the ambipolar potential, is what recovers the electron channel, and the modern axisymmetric-mirror programme — WHAM [36,37], the gas-dynamic trap [38,39,40], and Ryutov's reactor framing [11] — supplies the plug and end-cell physics the expander sits behind. Direct conversion is the piece of that revival not yet re-derisked at reactor scale.

THE OPERATING POINT IN CONTEXT

Table 8 places the burner's design operating point beside what the modern mirror programme has *demonstrated*, keeping the two categories strictly separate. The gas-dynamic trap raised its bulk electron temperature threefold, to ≈ 0.9 keV, and established the ambipolar-potential and electron-heating physics the plug relies on [38,39]; GAMMA-10 demonstrated travelling-wave deceleration of real mirror end-loss ions [30]; WHAM provides a published high-field HTS mirror physics basis and a beam-ion fusion-gain analysis [36,37]. The Kronos burner design point — $T_e = 89.72$ keV, $e\phi_i = 248.75$ keV, a $26.49\,\mathrm{T}$ plug, and a converter booked at 0.49 against a 0.70 design — sits two orders of magnitude above the demonstrated electron temperature, which is the honest measure of the reactor-scale extrapolation the plug and the converter both require. This paper's contribution is to make the converter side of that extrapolation explicit and bounded.

@>X L L L@ ATTRIBUTE	VALUE	BASIS	SOURCE
electron temperature (GDT)	≈ 0.9 keV	M	[38]
end-loss TWDEC deceleration (GAMMA-10)	demonstrated	M	[30]
beam direct converter recovery (100 kV)	$65 \pm 7\,\%$	M	[4]
high-field HTS mirror physics basis (WHAM)	published	M	[36]
electron temperature (burner)	89.72 keV	D	BU-L1-A1
plug potential (burner)	248.75 keV	D	BU-L1-A1
plug field (burner)	26.49 T	D	register

table continued

DEC efficiency (design / anchor)	0.70 / 0.49	D	BU-L1-A10
engineering gain	1.318	D	BU-L1-A1

AGAINST THE FUNDAMENTAL ADVANCED-FUEL LIMITS

Placing DEC in a recirculating balance situates it against Rider's fundamental limits on advanced-fuel systems near thermal equilibrium [24,25]. Because the burner recirculates a large fraction ($\varepsilon = 0.759$) to sustain the plug, the plant is honestly gated by that recirculation, and a converter improvement is a bounded lever rather than an escape from Rider's accounting. The same accounting is what motivates the colliding-beam and p–^{11}B alternatives [27,26], which trade the plug for a different non-equilibrium mechanism; the tandem-mirror line keeps a Maxwellian core and pays for it with the plug, which is why the plug — not the converter — is the binding gate.

§ 7

Design implications

THE DIRECTED-ELECTRON REFRAMING

The scientific novelty is the relocation of the DEC target. The standard framing follows the 14.68 MeV proton because it carries the birth energy; the slowing-down partition 10 shows that at reactor temperature that proton has already handed most of its energy to the electrons before it can be collected, so the dominant axial channel is a directed electron stream that no published converter recovers [10,2]. This reframing is robust across 20–200 keV (figure 7b) and names a testable open problem; the quasineutral two-species expander is one embodiment of its solution, scoped honestly as a bounded $\approx 13\,\%$ upside.

DEC AS A BOUNDED LEVER, AND THE HONEST GATE

The load-bearing design statement is that conversion is a bounded upside lever, not the closure mechanism. The net-positive knee sits at $\eta_{\text{dec}} \approx 0.52$, just above the frozen anchor; the global UQ puts every leading driver of Q_E in the confinement/plug set, not the converter (§5); and central-cell length, not η_{dec}, buys the net margin. The generator's honest gate is the recirculating plug power, and a bounded-negative experimental result on the converter would not threaten the machine — a separation that lets the converter be developed as an upside rather than a critical path.

THE HVDC-NATIVE PRODUCT EDGE

The converter's native-DC output is the product edge. For MetroVolt it deletes conversion stages and raises source-to-chip efficiency to 88.1 % while bounding fault energy at source (§4.7); for Aegis it enables a grid-independent black-start in $\approx 42\,\text{s}$ and millisecond islanded load-following. These are consequences of directness, not of a high converter efficiency, and they hold at the conservative 0.49 anchor.

AN UPSTREAM LEVER: ALPHA-CHANNELING

The recoverable charged fraction can, in principle, be raised upstream of the converter by RF alpha-channeling — a Fisch–Rax resonant wave that removes energy from the fast ions while transporting them toward the loss boundary [34,35], the inverse of the RF current-drive mechanism catalogued by Fisch [9]. In a worked embodiment a mode-converted channeling wave raises the recoverable charged fraction from a collisional baseline near 8 % to ≈80 % of the channelable fast-ion energy (figure 24), easing the recirculating burden that sets Q_E [59]. Like the converter, this is a bounded lever booked honestly: it improves the generator without being what closes it.

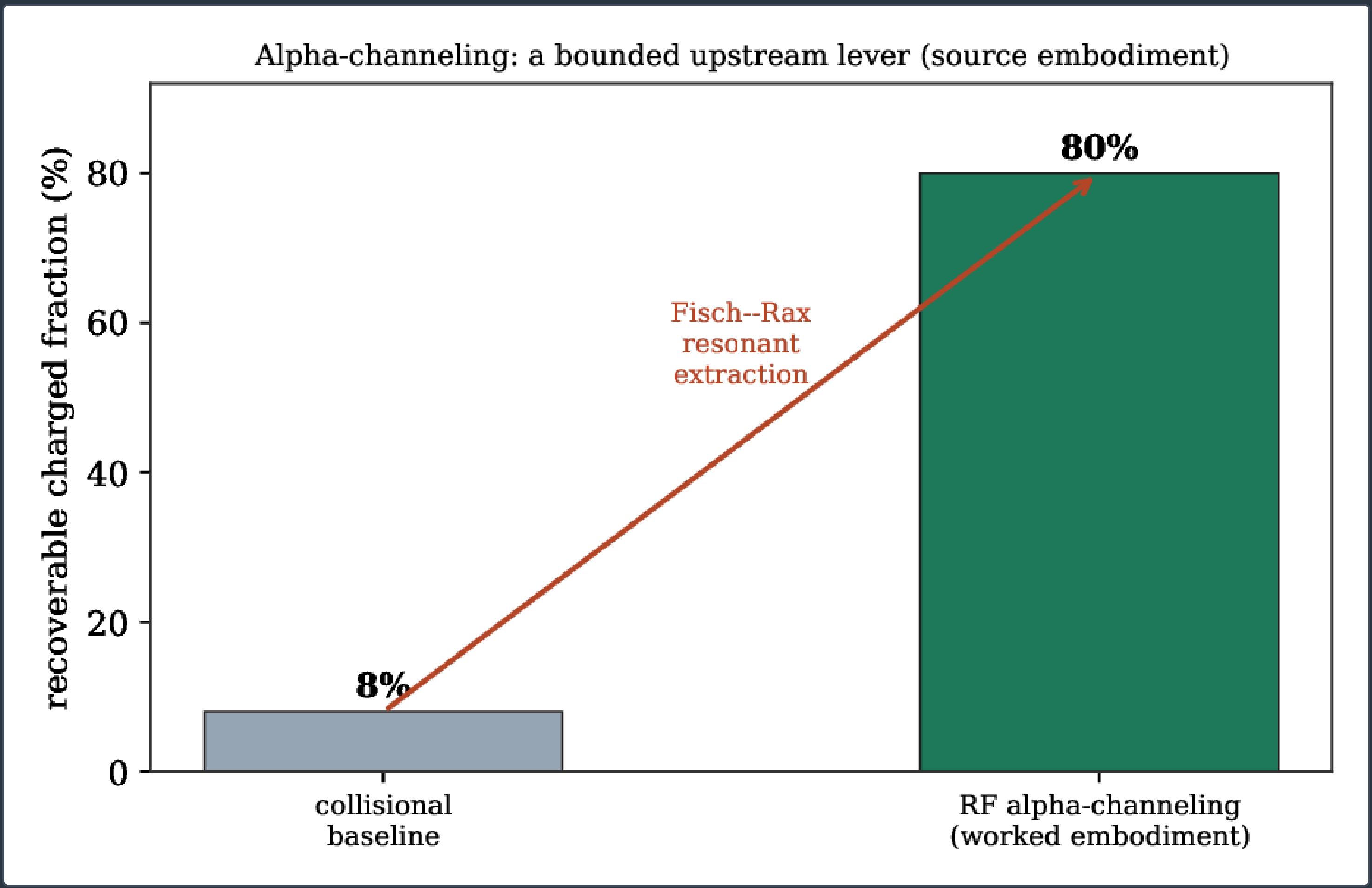

RF alpha-channeling as a bounded upstream lever [34,59]. A mode-converted channeling wave raises the recoverable charged fraction from a collisional baseline near 8 % to ≈80 % in the worked embodiment; it eases the recirculating burden that sets $Q_E = 1.318$. Source-embodiment output, not a measurement.

TWO DISTINCT MAGNETS

Finally, the two-magnet discipline must be kept. The burner's binding field is the 26.49 T plug coil, a distinct, higher-field magnet from the breeder's 16.84 T centrepost [51,1]; the plug microstability constraints [17] and the plug-coil engineering are carried by companion papers, and enter this paper only as the boundary condition that sets $e\phi_i$ and the end-loss spectrum.

§ 8

Limitations

Kronos has built no converter; every number here is a design target, a reproduced register anchor, or an open-risk model inference. The **0.49** anchor is a conservative measured travelling-wave tube efficiency, not a full-system plant measurement; the **≈ 28 %** expander electron recovery and the **55.5/44.5** axial split are worked-embodiment and model outputs, not measurements, and the split rests on booking the collisional partition against a finite confinement time 6. The space-charge and secondary-emission physics of a reactor-scale collector, and the neutron and thermal fatigue of the electrodes under the end-loss flux, are pre-registered follow-on items (grid erosion and lifetime, AG-CX-09/10 [1]) — the one honest open engineering gate on the converter. None of these bear on the generator's closure, which the plug gate — not the converter — governs; that separation is the paper's load-bearing honest statement.

§ 9

Future work and the experimental path

The converter's open items are pre-registered and scoped as bounded upsides, not as gates on the machine. Three experiments define the path. First, a velocity-buncher on the proton channel that narrows the beam below the travelling-wave acceptance $\Delta \approx 0.18$ 13: this would move the TWDEC from its raw-spread ≈ 0.51 toward the 0.75–0.80 pre-bunched figure, and its value is bounded because the electrostatic collector already meets the 0.70 design without it. Second, a bench-scale quasineutral two-species expander to test the electron-channel recovery of §2.8: the worked embodiment predicts $\approx 28\,\%$ recovery, and even a bounded-negative result closes the named directed-electron open problem 10. Third, a grid-erosion and lifetime run under a reactor-representative end-loss flux (AG-CX-09/10): this is the one honest engineering qualifier common to every electrostatic architecture (table 5), and it is coupled to the tantalum- and rhenium-free low-activation electrode down-select [61]. Upstream of all three, RF alpha-channeling (§7, figure 24) offers a further bounded lever on the recoverable fraction. None of these experiments is on the machine's critical path; each is an upside that the recirculating plug gate does not depend on, which is precisely why the converter can be developed as a research programme rather than a closure risk.

§ 10

Conclusion

For a D–^{3}He tandem-mirror burner the exhaust is overwhelmingly charged ($f_n = 5.44\,\%$), so its power can be recovered directly, without a thermal cycle on the direct channel. Writing the physics out, the axial loss at reactor temperature is dominated by a directed *electron* stream ($\approx 55.5\,\%$ against $\approx 44.5\,\%$ ions), inverting the birth-spectrum picture across $20\text{–}200$ keV, and no published converter recovers it; a quasineutral two-species expander is the inverse of the standard nozzle and returns a bounded $\approx 28\,\%$ of that channel. The converter efficiency is a ladder — frozen conservative anchor 0.49, design 0.70, ceiling 0.85 — and, placed in the recirculating balance, DEC is a bounded upside lever: the burner closes at $Q_E = 1.318$ and net $+850.0$ MWe, the net knee sits at $\eta_{\rm dec} \approx 0.52$, and closure is gated by the recirculating plug power, not by conversion. A $40{,}000$-sample global uncertainty study ($Q_E = 1.317 \pm 0.14$, $P(Q_E > 1) = 1.0$) and a Saltelli–Sobol attribution both put the leading drivers in the confinement/plug set, not the converter, and the synchrotron transport model — upstream of the converter — is the single load-bearing modelling choice. The direct, native-DC output is the product edge that gives MetroVolt an $88.1\,\%$ HVDC-native source-to-chip path and Aegis a $\approx 42\,$s grid-independent black-start. The reframing names and scopes an open problem in advanced-fuel energy conversion, and does so without letting the plant lean on it.

Acknowledgments tocsectionAcknowledgments Part of the Kronos Fusion Energy 2026 design series. The authors thank the Kronos physics de-risking programme for the frozen result set underlying every quantitative claim, and the NVIDIA GPU HPC campaign for the compute.

Reproducibility. Every headline quantity in this paper is a frozen anchor in the KRONOS Physics De-Risking Register[R0] (doi:10.5281/zenodo.22133057) and is regenerable from the archived toolkit and the uniquely named figure-generation scripts (`make_dec_figs_kfe14.py` and `make_dec_figs_kfe14_ext.py`) deposited with this paper; this paper is archived at doi:10.5281/zenodo.22645700; official version: https://www.kronosfusionenergy.com/publications/direct-energy-conversion.html. The power-balance chain (BU-L1-A10, BU-L1-A1), the efficiency ladder (BU-SX-01/03, ADJ3, BV-10), the collector staging (BV-10), the global UQ (KX-L1-A5-BU), and the product-fit figures (MV-CX-02/04/05, HX-07) are the load-bearing anchors. No result depends on unpublished or proprietary data, and no economic quantity appears.

Scope — what this paper does not claim. Kronos has built no converter; the recovered-fraction figures are worked-embodiment model outputs after modelled losses, not measurements, and direct energy conversion is a bounded upside lever, not the machine's closure mechanism.

Data availability tocsectionData availability This paper is archived at doi:10.5281/zenodo.22645700. Headline quantities are frozen anchors in the register [1] and cross the series: the Aegis burner [49], the MetroVolt burner [50], the REBCO plug and centrepost magnet basis [51], the recirculation-resolved Q_E closure [52], the collector-physics and converter-architecture studies [53,54], the end-cell/expander loss budget [55], the HVDC-native load interface and power-delivery topologies [56,57], the synchrotron-transport operating point [58], the RF alpha-channeling lever [59], the global sensitivity/UQ study [60], the tandem-mirror design-space mapping [62], and the low-activation electrode family [61]. Any economic analysis is reported separately and is not part of the public deposit.

Competing interests tocsectionCompeting interests Provisional patent applications relating to aspects of this work have been filed.

§ 11

Pastukhov confinement: derivation of the exponential barrier

Consider a species of temperature T_i confined by a mirror of ratio R and an electrostatic well of depth $e\phi_i \gg T_i$. Loss requires pitch-angle scattering into the loss cone *and* energy exceeding the barrier. In the high-barrier limit the escaping flux is dominated by particles near the barrier energy, and the bounce-averaged Fokker–Planck operator reduces, in the boundary layer, to a diffusion in pitch angle at fixed energy. Writing the loss rate as the diffusive flux out of the confined region and integrating over the near-barrier Maxwellian gives the confinement time

$$\tau_\parallel \simeq \tau_s\, g(R)\, \frac{e\phi_i}{T_i}\, \frac{\exp(e\phi_i/T_i)}{\ln(2R+1)},$$

where $\tau_s \propto T_i^{3/2}/n$ is the ion–ion collision time and $g(R)$ is an $O(1)$ mirror factor of weak R-dependence [12,13,14]. The exponential $\exp(e\phi_i/T_i)$ is the physically essential factor: for $e\phi_i/T_i = 2.764$ (design), $\exp(2.764) \approx 15.9$, so the barrier alone multiplies the mirror confinement by more than an order of magnitude. The linear prefactor $e\phi_i/T_i$ and the logarithmic mirror term are slowly varying corrections. This is the origin of the statement that the plug potential, not the converter, is the binding lever: Q_E is exponentially sensitive to $e\phi_i/T_i$ but only weakly sensitive to η_{dec}.

§ 12

The Bosch–Hale reactivity parameterization

The Maxwellian thermal reactivity is $\langle\sigma v\rangle = \int_0^\infty \sigma(E)\, v\, f_M(E)\, \mathrm{d}E$ with a relative-velocity Maxwellian f_M. Bosch and Hale fit the resulting integral to a Padé-type form 5 valid to within the experimental cross-section error over the quoted temperature ranges [23]. The coefficients used for figure 3 are collected in table 9; T is in keV and $\langle\sigma v\rangle$ in $\mathrm{cm^3\,s^{-1}}$. As a check, the parameterization returns $\langle\sigma v\rangle_{\mathrm{DT}}(64$ keV$) \approx 8.9 \times 10^{-16}$ and $\langle\sigma v\rangle_{\mathrm{D^3He}}(90$ keV$) \approx 1.5 \times 10^{-16}\,\mathrm{cm^3\,s^{-1}}$, consistent with the tabulated values.

	D–T	D–³HE	D–D (p)
B_G	34.3827	68.7508	31.3970
$m_r c^2$	1124656	1124572	937814
C_1	1.17302×10^{-9}	5.51036×10^{-10}	5.65718×10^{-12}
C_2	1.51361×10^{-2}	6.41918×10^{-3}	3.41267×10^{-3}
C_3	7.51886×10^{-2}	-2.02896×10^{-3}	1.99167×10^{-3}
C_4	4.60643×10^{-3}	-1.91080×10^{-5}	0
C_5	1.35000×10^{-2}	1.35776×10^{-4}	1.05060×10^{-5}
C_6	-1.06750×10^{-4}	0	0
C_7	1.36600×10^{-5}	0	0

Bosch–Hale coefficients 5 used in figure 3 [23]. B_G in keV$^{1/2}$, $m_r c^2$ in keV.

§ 13

The Stix critical energy and slowing-down partition

A fast ion of energy E and charge Z_1, mass m_1 slows on background electrons (temperature T_e) and ions. The electron drag scales as $\mathrm{d}E/\mathrm{d}t|_e \propto E$ (constant electron collision frequency for $v_1 \ll v_{te}$), while the ion drag scales as $\mathrm{d}E/\mathrm{d}t|_i \propto E^{-1/2}$. The two are equal at the critical energy [18],

$$E_c = \left(\frac{3\sqrt{\pi}}{4}\right)^{2/3} \frac{m_1}{m_e^{1/3}} \left(\sum_j \frac{n_j Z_j^2}{n_e m_j}\right)^{2/3} T_e \simeq 14.8\, T_e \left(\frac{\bar{A}^{2/3}}{Z_{\mathrm{eff}}}\right),$$

with $\bar{A}$ the background mean mass number and Z_{eff} the effective charge. Writing $x = E/E_c$, the fraction of energy going to ions as the particle slows from E_0 to rest is

$$G\left(\frac{E_0}{E_c}\right) = \frac{E_c}{E_0} \int_0^{E_0/E_c} \frac{\mathrm{d}y}{1 + y^{3/2}},$$

so the electron share is $f_e = 1 - G$ 10. For $E_0/E_c \gg 1$ the integral grows only as $(E_0/E_c)^{1/3}$, so $G \to 0$ and $f_e \to 1$: a fast ion born far above critical dumps almost all its energy on the electrons. At $E_0/E_c \approx 11$ (the 14.68 MeV proton at $T_e = 89.7$ keV) numerical evaluation of 22 gives $G \approx 0.17$, hence $f_e \approx 0.83$. Booking f_e against the finite $\tau_\parallel$ of 20 — the ion is lost before it fully thermalizes — yields the thermalized axial split of figure 7.

§ 14

The Child–Langmuir space-charge limit

For a planar diode of gap d with a retarding potential V and a decelerated species of charge e, mass m, Poisson's equation with the space-charge-limited boundary condition ($E = 0$ at the emitting plane) is $\mathrm{d}^2\phi/\mathrm{d}x^2 = -\rho/\varepsilon_0$ with $\rho = J/v(x)$ and $\frac{1}{2}mv^2 = e[V - \phi(x)]$. Substituting and integrating twice with $\phi(0) = 0$, $\phi(d) = V$, $\phi'(0) = 0$ gives the maximum steady current density 12,

$$J_{\mathrm{CL}} = \frac{4\varepsilon_0}{9}\sqrt{\frac{2e}{m}}\,\frac{V^{3/2}}{d^2}$$

[28]. For protons at $V = 428$ keV across $d = 5\,\mathrm{cm}$, $J_{\mathrm{CL}} \approx 4 \times 10^3\,\mathrm{A\,m^{-2}}$; the raw throat current density is far larger, so the flux-expansion ratio R_{exp} must be chosen so that $J_{\mathrm{throat}}/R_{\mathrm{exp}} < J_{\mathrm{CL}}$ before the beam reaches the electrodes (figure 9). This is the quantitative reason electrostatic DEC at reactor power requires the expander.

§ 15

Collector-stage optimization

For a spectrum $g(E)$ over $[E_{\min}, E_{\max}]$ and N electrodes at potentials $V_1 < \cdots < V_N$, the collected work per incident particle is $\sum_k eV_k \int_{eV_k}^{eV_{k+1}} g\,\mathrm{d}E$; the collector efficiency 11 is that work divided by the incident energy $\int Eg\,\mathrm{d}E$, times the grid factor $\eta_{\text{grid}} = 0.93$. Maximising over $\{V_k\}$ is a one-dimensional dynamic program: the optimal boundaries place each electrode so that the residual heat $E - eV_k$ dumped by the particles it collects is minimised, which for a smooth g spaces the electrodes more finely where g is large. Solving this program over the end-loss spectrum (figure 8) gives $\eta_{\text{coll}} = 0.70$ at $N = 3$, 0.83 at $N = 6$, and asymptotes toward the grid ceiling; a fully graded profile ($N = 10$–13) reaches the design value robustly across the load range (figure 15, figure 18). The optimization, the secondary-emission model, and the space-charge-limited grid optimum are developed at length in the companion collector-physics paper [53].

§ 16

Numerical schemes and convergence

The kinetic converter models use an explicit electromagnetic particle-in-cell scheme (WarpX/SMILEI): fields on a Yee grid, current deposition by charge-conserving Esirkepov weighting, and a Boris particle push that is time-reversible and second-order accurate. Stability requires the Courant condition $c\Delta t < \Delta x/\sqrt{D}$ in D dimensions and resolution of the Debye length, $\Delta x \lesssim \lambda_D$, to avoid grid heating. The slowing-down partition uses a 1-D Fokker–Planck solver on Rosenbluth potentials with an implicit (backward-Euler) step in energy, unconditionally stable and first-order in time [19,21]. Convergence is verified by refinement (figure 12): the collector efficiency 11 is stable to the third digit for $\gtrsim 128$ cells per Debye length, and the energy-conservation error of the Boris push falls as $(\omega_{pe}\Delta t)^2$, confirming second-order temporal accuracy. The 0-D closure is reproduced byte-for-byte against the frozen register anchor, and a matrix-product-state kinetic solver provides an independent cross-check of the distribution function [52].

§ 17

Parameter table

Table 10 collects the frozen parameters used throughout, with their register serials.

@L L L >X@ PARAMETER	SYMBOL	VALUE		SERIAL
fusion power	P_{fus}	4298.5	MW	BU-L1-A1
neutron fraction	f_n	5.44 %		BU-L1-A1
neutron power	P_n	233.95	MW	BU-L1-A1
plug potential	$e\phi_i$	248.75	keV	BU-L1-A1
barrier ratio	$e\phi_i/T_i$	2.764		BU-L1-A1
electron temperature	T_e	89.72	keV	BU-L1-A1
bremsstrahlung	P_{brems}	743.10	MW	BU-L1-A1
synchrotron (reabsorbed)	P_{syn}	1803.04	MW	BU-L1-A1
synchrotron cutoff harmonic	n^*	≈ 10.4		AG-DR-01
wall reflectivity (required)	R_w	$\gtrsim 0.83$		AG-DR-01
charged axial end-loss	P_{ax}	2719.7	MW	BU-L1-A10
end-loss mean / spread	$\bar{E}$	428	keV / $\approx 34\,\%$	BV-10
DEC efficiency (design)	η_{dec}	0.70		BU-L1-A10
DEC efficiency (frozen anchor)	η_{dec}	0.49		BU-SX-01
grid sub-efficiency	η_{grid}	0.93		BV-10
thermal-cycle efficiency	η_{th}	0.45		BU-L1-A10
gross electric	P_{out}	3522.0	MWe	BU-L1-A10
recirculating input	P_{in}	2672.0	MWe	BU-L1-A10
net electric	net	+850.0	MWe	BU-L1-A10
recirculating fraction	ε	0.759		BU-L1-A10
engineering gain	Q_E	1.318		BU-L1-A1
global-UQ gain	Q_E	1.317 ± 0.14		KX-L1-A5-BU
plug field (burner)	B_{plug}	26.49 T		register
centrepost field (breeder)	B_{cp}	16.84 T		register

Frozen burner and DEC parameters (register anchors [1]).

tocsectionReferences

APPARATUS

Portfolio, People & Record

The intellectual-property estate, the people who built it, the limitations that gate it, and the sources it rests on.

1	4	40	27
GRANTED PATENT	2026 PROVISIONALS	TEAM MEMBERS	2022 PROVISIONALS

INTELLECTUAL PROPERTY

The patent portfolio

The estate spans a granted high-field magnet patent, pending utility and 2026 provisional filings that map to the two products, a digital-twin control provisional, a registered trademark application, and the original 2022 provisional family. Every patentable disclosure in the five-paper arXiv drop was protected **before** publication: the breeder and burner provisionals were filed 1–2 August, and a publication-gap omnibus filing the evening before the drop swept up the DEC, plasma-control, and REBCO-winding matter of the three otherwise-unprotected papers. Patent numbers and application serials are matters of public record; claim scope is summarised, not reproduced.

GRANTED & PENDING UTILITY

US 12,009,112	High-field tilted graded-REBCO magnet architecture (KRONO-002A) · *app. 17/878,550*	GRANTED
US 17/878,507	Core device / method (KRONO-001A) · *utility*	PENDING

2026 PROVISIONAL FILINGS — MAPPED TO THE PRODUCTS

64/124,209	Hyperion — spherical-tokamak tritium / helium-3 foundry · *breeder · filed Aug 2026*	FILED
64/124,220	Aegis / MetroVolt — synchrotron-cutoff, fuel-selection & plug-winding · *generator · filed Aug 2026*	FILED
64/115,167	KRONOS-CTRL digital-twin plant control · *provisional · filed Jul 2026*	FILED
64/005,440	Integrated spherical-tokamak fusion architecture · *early integrated-architecture filing · filed Mar 2026*	FILED
64/105,530	Negative-triangularity spherical-tokamak architecture · *foundational ST filing · filed Jul 2026*	FILED
64/128,097	Publication-gap omnibus — quasineutral two-species expander DEC · provenance-gated / latency-split plasma control · as-built high-field winding & conductor architecture · *filed 7 Aug 2026, the evening before the arXiv drop*	FILED

TRADEMARK & ORIGIN

FTK-98801894	Kronos Fusion Energy — trademark application	FILED
KR-2022-*	Original provisional family (KR-2022-00001 … 00027) · *27 filings, 2022*	PRIORITY

The narrow, defensible magnet novelty — the specific conductor and the digital-twin winding optimisation, not high-field REBCO as a category — is the commercial core that can earn ahead of any Q > 1 milestone, with markets in fusion magnet supply, MRI/NMR, accelerators, and proton therapy. The claim is scoped honestly: the high field is a *system field* result, not a stand-alone-coil record; the small-bore plug coil is structurally infeasible as a bare winding but resolved by a stress-managed structural shield (feasible-pending-FEA); and the winding-tape experiment returned a *null result*. The value is the method, not a field record.

THE TEAM

Founding partners, board, advisors & auditors

Kronos is built by a bench of advanced-fuel-fusion, high-field-magnet, direct-conversion, and materials specialists, with a board and operations team drawn from defense, national laboratories, and industry. Dates are shown as ranges; where a tenure has ended or is term-ending, the range says so.

FOUNDING PARTNERS — SCIENCE

Dr. Gerald Kulcinski
Co-Founder · Helium-3 & Advanced-Fuel Fusion
UW–Madison · 2023–Present

Dr. Carl Weggel
Chief Scientist / S.M.A.R.T. Design
MIT Alcator Program · 2022–Present

Dr. Robert J. Weggel
Magnetic Field Design
MIT Magnet Lab · 2022–Present

BOARD

Priyanca Ford
Founder & CEO · Executive Board
2022–Present

Bandel Carano
Finance / Strategy
Oak Investment Partners / Stanford · 2025–2026

Patrick Schweiger
Fusion Device Engineering
Oklo / CFS / TerraPower · 2025–Present

SCIENTIFIC ADVISORS

Dr. Steven O. Dean
Fusion Policy & History
DOE / Fusion Power Associates · 2025–Present

Dr. Patrick H. Diamond
Plasma Turbulence & Transport
UC San Diego · 2025–Present

Dr. Jack J. Dongarra
HPC & Numerical Algorithms
Turing Award · 2025–Present

Dr. Nasr M. Ghoniem
Chief Material Scientist
UCLA · 2025–Present

Dr. Siegfried Glenzer
Plasma Physics & Laser Fusion
Stanford / SLAC · 2022–Present

Dr. David A. Hammer
Pulsed-Power Fusion
Cornell · 2025–Present

Dr. Donald A. Spong
Plasma Theory & Confinement
ORNL · 2025–Present

Dr. Curtis Smith
Risk Assessment & Nuclear PRA
MIT / Idaho National Lab · 2025–Present

RADM (Ret.) David Goggins
Naval Engineering & Power-Plant Design
U.S. Navy · 2023–2026

Dr. Konstantin Batygin
Mathematician
Caltech · 2022–2025

Dr. Ruben Fair
Magnet Design / ITER Liaison
PPPL / Jefferson Lab · 2022–2025

Dr. Paul S. Weiss
Materials & Nanotechnology
UCLA · 2022–2025

SCIENTIFIC AUDITORS

Dr. Wilfred A. Cooper
Plasma Equilibrium Theory
EPFL / Swiss Plasma Center · 2025–Present

Dr. Ahmed Hassanein
Plasma–Material Interactions
Purdue / Argonne · 2025–Present

Dr. Patrick E. Hopkins
Extreme Thermal Materials
U. of Virginia · 2025–Present

Dr. Peter Hosemann
Materials Joining & Structural Integrity
UC Berkeley · 2025–Present

Dr. Travis W. Knight
Advanced Nuclear Fuels & Systems
U. of South Carolina · 2025–Present

Dr. Philippe Lebrun
Cryogenics & Magnet Cooling
CERN · 2025–Present

Dr. Nitendra Singh
Nuclear Safety & Fuel Cycle
ITER · 2025–Present

Dr. Guido Van Oost
Magnetic Confinement & Fusion Systems
Ghent University · 2025–Present

Dr. Gary S. Was
Radiation Materials & Structural Integrity
U. of Michigan · 2025–Present

Dr. Ray Sedwick
Direct Energy Conversion
U. of Maryland · 2025

OPERATIONS

Michael Laughlin
Chief Operating Officer
2022–Present

Martin Owens
Chief Strategy Officer
LANL / GE Hitachi · 2022–Present

MG (Ret.) Paul Pardew
Chief Contracting Officer
Army Contracting Command · 2022–Present

David Beck
Fusion Commercialization
U.S. Space Force · 2024–Present

Sushma Bhatia
Environmental & Legislative
Google · 2022–Present

Michael De Frenza
Technology Licensing
2023–Present

MG (Ret.) Robin L. Fontes
Cybersecurity & Defense
Army Cyber Command · 2022–Present

Vijay Gehani
Supply Chain & Components
INOX India · 2024–Present

Jon Michel Greenwood
IT & AI Infrastructure
Live Nation · 2023–Present

Brian C. O'Neill
National Security
CIA / ODNI · 2022–Present

Gen. (Ret.) Gustave F. Perna
DoD Liaison
Operation Warp Speed · 2022–2023

Andrea Romero
Marketing Lead
2022–Present

Legal counsel is retained; those roles are held on the internal roster and are not listed here.

SOURCES

References

1 P I Ford, *KRONOS Physics De-Risking Register*, v8, Kronos Fusion Energy 2026 series. doi:10.5281/zenodo.22133057

2 R W Moir and W L Barr, Venetian-blind direct energy converter for fusion reactors, *Nucl. Fusion* **13** 35 (1973). doi:10.1088/0029-5515/13/1/005

3 W L Barr and R W Moir, Test results on plasma direct converters, *Nucl. Technol./Fusion* **3** 98 (1983).

4 W L Barr, G W Hamilton and R W Moir, Experimental results from a beam direct converter at 100 kV, *J. Fusion Energy* **2** 131 (1982). doi:10.1007/BF01054580

5 R F Post, Mirror systems: fuel cycles, loss reduction and energy recovery, in *Nuclear Fusion Reactors* (British Nuclear Energy Society, London, 1970) p. 88.

6 G H Miley, *Fusion Energy Conversion* (American Nuclear Society, La Grange Park, IL, 1976).

7 T Kammash, *Fusion Reactor Physics: Principles and Technology* (Ann Arbor Science, Ann Arbor, MI, 1975).

8 D E Baldwin, End-loss processes from mirror machines, *Rev. Mod. Phys.* **49** 317 (1977). doi:10.1103/RevModPhys.49.317

9 N J Fisch, Theory of current drive in plasmas, *Rev. Mod. Phys.* **59** 175 (1987). doi:10.1103/RevModPhys.59.175

10 R F Post, The magnetic mirror approach to fusion, *Nucl. Fusion* **27** 1579 (1987). doi:10.1088/0029-5515/27/10/001

11 D D Ryutov, Open-ended traps, *Sov. Phys. Usp.* **31** 300 (1988). doi:10.1070/PU1988v031n04ABEH005747

12 V P Pastukhov, Collisional losses of electrons from an adiabatic trap in a plasma with a positive potential, *Nucl. Fusion* **14** 3 (1974). doi:10.1088/0029-5515/14/1/001

13 R H Cohen, M E Rensink, T A Cutler and A A Mirin, Collisional loss of electrostatically confined species in a magnetic mirror, *Nucl. Fusion* **18** 1229 (1978). doi:10.1088/0029-5515/18/9/005

14 D E Baldwin and B G Logan, Improved tandem mirror fusion reactor, *Phys. Rev. Lett.* **43** 1318 (1979). doi:10.1103/PhysRevLett.43.1318

15 G I Dimov, V V Zakaidakov and M E Kishinevsky, Thermonuclear confinement with twin mirror systems, *Sov. J. Plasma Phys.* **2** 326 (1976).

16 T K Fowler, R W Moir and T C Simonen, A new simpler way to obtain high fusion power gain in tandem mirrors, *Nucl. Fusion* **57** 056014 (2017). doi:10.1088/1741-4326/aa5e54

17 R F Post and M N Rosenbluth, Electrostatic instabilities in finite mirror-confined plasmas, *Phys. Fluids* **9** 730 (1966). doi:10.1063/1.1761740

18 T H Stix, Heating of toroidal plasmas by neutral injection, *Plasma Phys.* **14** 367 (1972). doi:10.1088/0032-1028/14/4/002

19 M N Rosenbluth, W M MacDonald and D L Judd, Fokker–Planck equation for an inverse-square force, *Phys. Rev.* **107** 1 (1957). doi:10.1103/PhysRev.107.1

20 B A Trubnikov, Particle interactions in a fully ionized plasma, *Rev. Plasma Phys.* **1** 105 (1965).

21 J Killeen and K D Marx, The solution of the Fokker–Planck equation for a mirror-confined plasma, *Methods in Computational Physics* **9** 421 (1970).

22 L Spitzer, *Physics of Fully Ionized Gases*, 2nd ed. (Interscience, New York, 1962).

23 H-S Bosch and G M Hale, Improved formulas for fusion cross-sections and thermal reactivities, *Nucl. Fusion* **32** 611 (1992). doi:10.1088/0029-5515/32/4/I07

24 T H Rider, Fundamental limitations on plasma fusion systems not in thermodynamic equilibrium, *Phys. Plasmas* **4** 1039 (1997). doi:10.1063/1.872556

25 W M Nevins, A review of confinement requirements for advanced fuels, *J. Fusion Energy* **17** 25 (1998). doi:10.1023/A:1022513215080

26 W M Nevins and R Swain, The thermonuclear fusion rate coefficient for p–^{11}B reactions, *Nucl. Fusion* **40** 865 (2000).

COLOPHON

How this document was made

The Kronos Fleet — Combined Editorial, 2026 is set in **Fraunces** (display), **Gelasio** (text), and **IBM Plex Mono** (data & equations), carried forward from the Kronos editorial design system.

The figures are rendered at 300 dpi from the deposited generator scripts; the document is composed as a single self-contained file with embedded fonts and imagery, paginated to US Letter, and rendered to PDF through a headless Chromium engine in matched light and dark editions.

Every headline quantity carries an evidence class; withdrawn and restated values are marked as such. Nothing herein is frozen beyond the founder-approved Tier-A set.

Explore it live — turn the interactive 3-D model, run the deposited solvers in the physics validator, and watch the companion film series.

LEGAL NOTICE

Notice, status, and distribution

Conceptual design & simulation study. This document reports a conceptual design and simulation study. It is not a construction commitment, a safety-analysis report, a regulatory filing, or an offer of securities. Forward-looking statements — schedules, costs, market sizes, and performance — are estimates subject to the limitations set out in the Simulations part and may change.

Numbers and their classes. Quantities are reported with evidence classes and case labels; modelled, assumed, and requirement-class values are identified as such and are not to be quoted without their labels.

Public edition. This edition carries the physics and design only; all financial, funding, and defense-commercial content has been removed for public distribution. The scientific text corresponds to the arXiv and journal submissions.

THE 2026 KRONOS SERIES

One programme, many papers

This editorial is one paper in the Kronos 2026 series — a real fusion company's complete, reproducible physics record for a spherical-tokamak breeder and its low-neutron D–^{3}He tandem-mirror burners. Every headline number is a frozen anchor in the Physics De-Risking Register.

Explore the whole programme: the De-Risking Register, the interactive 3-D model, and the physics validator.

KRONOS FUSION ENERGY

Direct Energy Conversion for a D–^{3}He Tandem-Mirror Burner: Recovering Charged-Particle Power Directly Without a Thermal Cycle

A real fusion company building real machines. Explore the science, live.

Zenodo · doi:10.5281/zenodo.22645700

Read on kronosfusionenergy.com

The Physics De-Risking Register